nature neuroscience

Hippocampal global remapping for different sensory modalities in flying bats

Maya Geva-Sagiv[1,2], Sandro Romani[3], Liora Las[1] & Nachum Ulanovsky[1]

Hippocampal place cells encode the animal's spatial position. However, it is unknown how different long-range sensory systems affect spatial representations. Here we alternated usage of vision and echolocation in Egyptian fruit bats while recording from single neurons in hippocampal areas CA1 and subiculum. Bats flew back and forth along a linear flight track, employing echolocation in darkness or vision in light. Hippocampal representations remapped between vision and echolocation via two kinds of remapping: subiculum neurons turned on or off, while CA1 neurons shifted their place fields. Interneurons also exhibited strong remapping. Finally, hippocampal place fields were sharper under vision than echolocation, matching the superior sensory resolution of vision over echolocation. Simulating several theoretical models of place-cells suggested that combining sensory information and path integration best explains the experimental sharpening data. In summary, here we show sensory-based global remapping in a mammal, suggesting that the hippocampus does not contain an abstract spatial map but rather a 'cognitive atlas', with multiple maps for different sensory modalities.

The hippocampus is important for declarative and spatial memories[1,2] and has been suggested to hold a 'cognitive map' of the environment[1]. This notion is supported by the existence of place cells, pyramidal neurons exhibiting place-specific activity, which are reported in rodents[1,3–5], primates[6,7] and bats[8–11]. Importantly, place cells in rodents remap when the animal is transferred between different rooms[4], suggesting different hippocampal maps for different environments. However, it is unknown whether the same environment is represented by one abstract map when two different sensory systems are used, or whether the brain creates different spatial representations for different sensory situations. Indeed, because animals may perceive and use different constellations of landmarks for navigating in daylight versus nighttime, these differences in the perceived sensory world could potentially translate to differences in hippocampal maps.

To test whether different senses lead to different spatial maps, it is important to cleanly dissociate these senses. The few studies that explored this question in rodents yielded conflicting results[12–14], possibly because perfect sensory dissociation is difficult to achieve in freely running rats because of their predominant proximal senses: olfaction and somatosensation via whisking. These proximal senses are active regardless of the light level and are difficult to control for. Here we conducted experiments in an animal that possesses two high-resolution sensory systems that are easier to control, the Egyptian fruit bat[15–18]. These bats have excellent long-range senses, vision and echolocation, and these senses can be turned on or off by changing the light level[19]. This enabled us to design an experimental setup that allows clean dissociation between these two sensory systems.

Bats flew within the same space and performed the same behavioral task, using either one sense or the other. We recorded neurons in hippocampal areas CA1 and subiculum; the subiculum is the major output station of the hippocampus, for which previous studies in rats provide conflicting accounts of hippocampal remapping[20,21]. Spatial representations in the bat hippocampus were very different under the two sensory conditions, exhibiting a strong instance of global remapping. This remapping was observed not only in pyramidal cells but also in interneurons. Remapping differed dramatically between the two hippocampal subregions: in the subiculum, most neurons were active in only one of the sensory conditions ('on/off global remapping'), while in CA1, neurons shifted their place fields ('shift-based global remapping'). These results suggest that the hippocampus does not contain a single abstract spatial map for a given environment, but rather contains multiple maps for different sensory modalities, for which we propose a notion of a hippocampal 'cognitive atlas'.

RESULTS

We trained seven Egyptian fruit bats to fly back and forth along a 1.5-m linear flyway embedded in a three-dimensional (3D) room (2.5 × 1.7 × 2.5 m) and obtain food from a landing ball placed in one of nine possible positions at each end of the flyway (**Fig. 1a**; Online Methods). We used a tetrode-based microdrive and a tethered headstage to record neurons in hippocampal areas CA1 and subiculum (**Fig. 1a**,**b**). Pyramidal cells were separated from fast-spiking interneurons on the basis of spike width and firing rate[22] (**Fig. 1c**). We collected a total of 53 place cells in CA1 and 41 place cells in the subiculum, as well as 34 interneurons (Online Methods). In CA1, 63% of the pyramidal neurons were place cells; and in the subiculum, 38% of the neurons were place cells. These percentages are similar to the percentages of place cells reported in rat CA1 and subiculum[3,20,21,23] (Online Methods). The firing rates of place cells were higher during flight than the rates found in previous studies on crawling bats[10,24],

[1]Department of Neurobiology, Weizmann Institute of Science, Rehovot, Israel. [2]Edmond and Lily Safra Center for Brain Research, Hebrew University, Jerusalem, Israel. [3]Howard Hughes Medical Institute, Janelia Research Campus, Ashburn, Virginia, USA. Correspondence should be addressed to N.U. (nachum.ulanovsky@weizmann.ac.il) or L.L. (liora.las@weizmann.ac.il).

Received 2 March; accepted 24 April; published online 30 May 2016; corrected online 7 June 2016 (details online); doi:10.1038/nn.4310

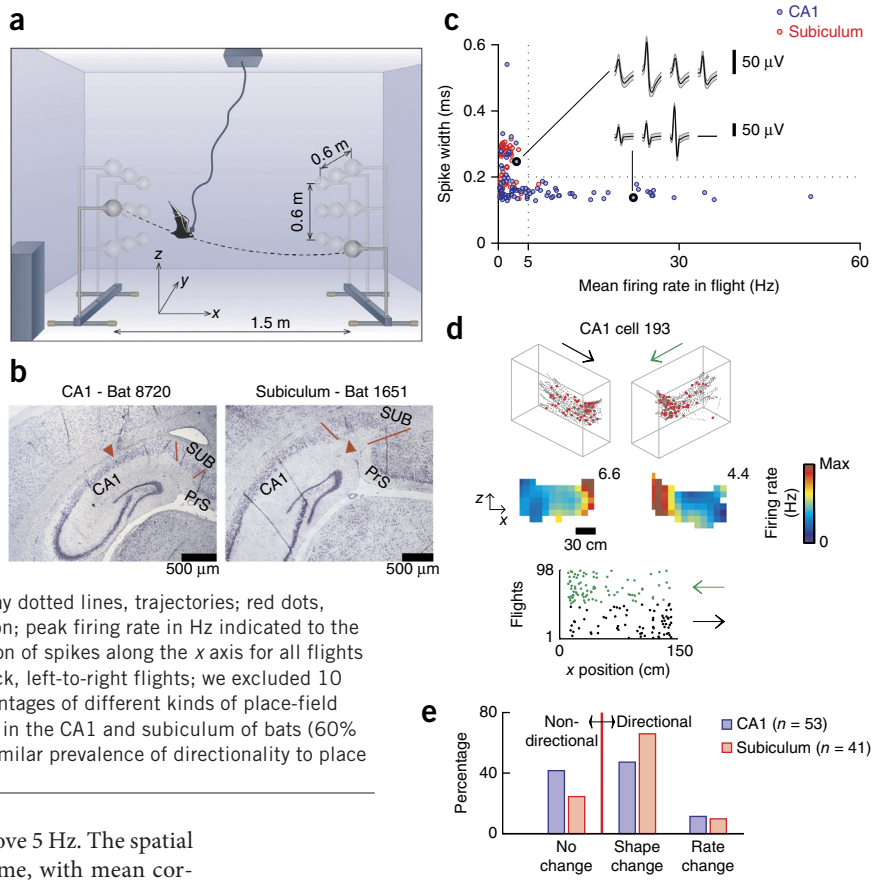

Figure 1 Neural recordings from CA1 and subiculum of bats flying along a linear flyway. (**a**) Behavioral setup. Egyptian fruit bats flew back and forth along a linear flyway, landing on a ball placed in one of nine possible locations at each end; the landing ball was moved randomly after every flight lap. (**b**) Coronal sections through dorsal hippocampal areas CA1 (left) and subiculum (right). Arrowheads, tetrode tracks; red lines, borders of CA1, subiculum (SUB) and presubiculum (PrS). (**c**) Separation of putative pyramidal cells (mean firing rate < 5 Hz) and interneurons (firing rate > 5 Hz and spike width < 0.2 ms). Example waveforms are shown for the four channels of a tetrode (mean ± s.d.), for a CA1 pyramidal cell (top) and CA1 interneuron (bottom); these two cells are also marked by black circles on the scatterplot. (**d**) Example cell from CA1 exhibiting different place fields for the two flight directions. Columns depict left-to-right flights or right-to-left flights (see arrows) for a single behavioral session. Top row: raw data (gray dotted lines, trajectories; red dots, spikes). Middle row: 2D firing-rate maps, *xz* projection; peak firing rate in Hz indicated to the right of each map. Bottom row: raster showing position of spikes along the *x* axis for all flights (*y* axis); green, spikes during right-to-left flights; black, left-to-right flights; we excluded 10 cm of the *x* axis near the balls at each end. (**e**) Percentages of different kinds of place-field directionality (see Online Methods). Most place cells in the CA1 and subiculum of bats (60% and 75%, respectively) were directionally tuned: a similar prevalence of directionality to place cells in rats running along a linear track[21,23,25].

with many place cells having peak firing rates above 5 Hz. The spatial tuning of place cells was highly stable across time, with mean correlation of $r = 0.80$ between firing-rate maps for the odd versus even minutes of a session (**Supplementary Fig. 1**).

As in rats running on linear tracks[21,23,25], we found that the majority of 3D place cells in bats flying along a linear flyway were directionally tuned (CA1: 58%, subiculum: 75%; **Fig. 1d**,**e** and **Supplementary Fig. 2**). Again as in rats[21,23], the directionality was expressed either by shifts of place-field position or by shutdown of firing in one of the flight directions (**Fig. 1e** and **Supplementary Fig. 2**). The positions of place fields over-represented the reward sites (landing balls) as compared to the center of the flyway (**Supplementary Fig. 3a**), similarly to the over-representation of reward location by hippocampal place fields in rats[26]. We did not find any systematic relation between place-field positions in the two flight directions; and, in particular, we found no evidence for distance coding[27] (**Supplementary Fig. 4**).

Switching sensory modalities elicits place-cell remapping

To examine whether a switch of sensory modality could elicit remapping in place cells, we compared neural activity under vision versus under echolocation while verifying clean sensory dissociation. We conducted daily recordings from hippocampal neurons in a Light–Dark–Light′ design, where the Light′ condition was a repetition of the first Light (vision) condition (**Fig. 2a**). Multiple objects in the room served both as visual cues and as sonar cues (e.g., cabinet, cable commutator box, cameras, speakers and printed paper images hanging on the acoustic foam; see **Fig. 2a**). The bat was not disconnected from the recording cable between sessions and remained continuously inside the room across all the sessions. Between behavioral sessions, the bat was placed in a cage positioned in the middle of the behavioral arena; during these periods, the bats were awake and often moved around (**Supplementary Fig. 5e**), and had a full view of the room (Online Methods). The two Light sessions (vision-based) were conducted under 2 lux illumination, a level at which Egyptian fruit bats are known to dramatically reduce the rate and amplitude of their echolocation clicks[19,28]. To ensure complete masking of echolocation, we also broadcasted loud broadband noise during the Light sessions. The Dark session (echolocation-based) was conducted in complete darkness (illuminance 10^{-6} lux). In all sessions, we used ventilators to eliminate mid-air odor trails. We conducted behavioral tests to verify the double dissociation between vision and echolocation in the two conditions (**Supplementary Fig. 5a**), and we also verified that flight velocity and spatial coverage were similar under the two conditions (**Supplementary Figs. 5b**,**c** and **6d**,**e**).

We analyzed 56 neurons from CA1 and 27 neurons from subiculum, separated into the two flight directions. These neurons were included on the basis of spike-sorting stability (stable clusters between all rest sessions) and tuning stability between Light sessions (two-dimensional (2D) firing-rate map correlation between Light and Light′ sessions: $r > 0.5$); 89% of these cells were significant place cells (based on a 95% shuffling criterion for the spatial information; see Online Methods). The percentage of cells in CA1 that passed both the spike-sorting stability criterion and the tuning-stability criterion was almost two-fold higher than in the subiculum (63% of cells were stable in CA1 versus 33% in the subiculum) — in line with results of previous studies on rats, which found that subiculum cells tend to be less functionally stable[20].

Many of the place cells exhibited clear remapping between vision-based and echolocation-based conditions. Some cells were active in only one of the sensory conditions (**Fig. 2b**,**c**). Some cells shifted their firing field between the two sensory modalities (**Fig. 2d**–**f**). Other cells kept a relatively stable firing field under both sensory modalities (**Fig. 2g**).

Notably, a very large fraction of subicular cells were active in only one sensory modality: 59% of the subiculum cells (16 of 27) consistently

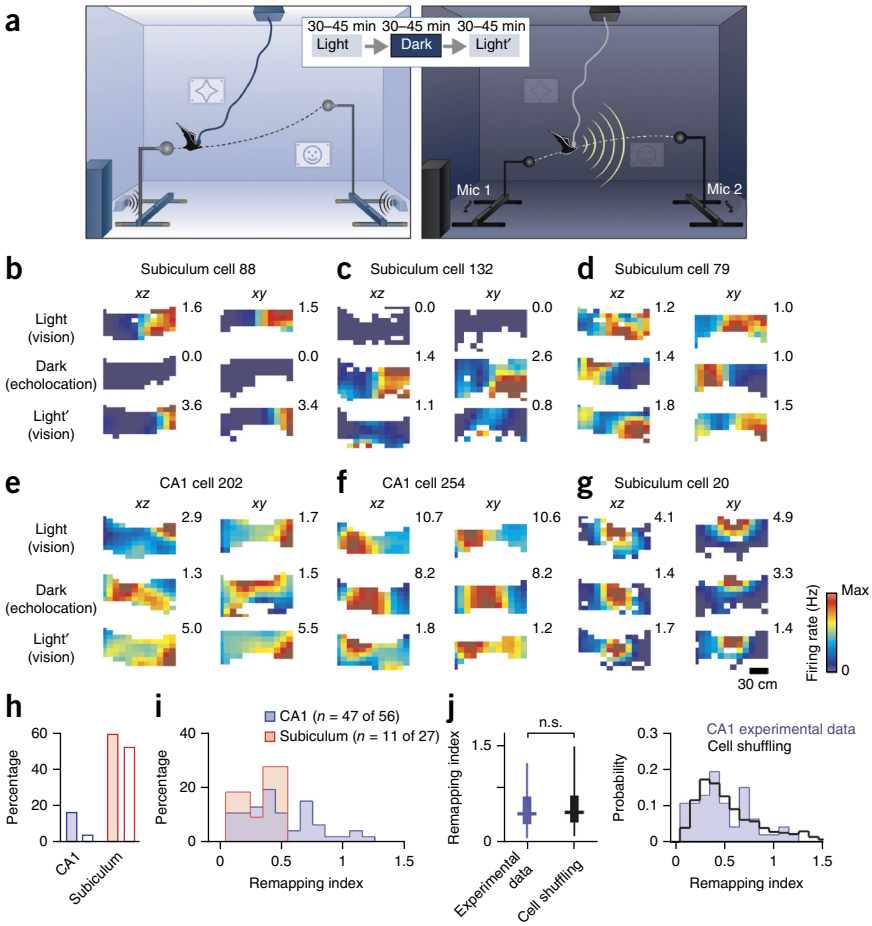

Figure 2 Switching sensory modalities elicits strong place-cell remapping. (**a**) Schematic of experimental design: vision-based sessions ('Light', left) and echolocation-based session ('Dark', right). Two speakers broadcasted loud broadband noise in the light sessions (but not in the dark session), in order to mask echolocation. Salient landmarks in the room served as both visual and echo-reflecting landmarks: cabinet, cable commutator box and paper drawings hung on the foam walls. (**b**–**g**) Six example cells from CA1 and subiculum. For each cell, columns depict *xz* and *xy* projections and rows depict behavioral sessions (vision–echolocation–vision′). 2D rate-maps plotted as in **Figure 1d**. (**h**) Percentage of cells active only in one modality, in CA1 (blue) and subiculum (red). Filled bars, data based on our standard spike-count threshold to define an active neuron (Online Methods); empty bars, using a lower threshold of 15 spikes per session. Most subiculum cells were active in only one modality, while CA1 cells were active in both. (**i**) Distribution of remapping index ($1 - r_{2D}$, where r_{2D} is the 2D Pearson correlation; see Online Methods for details) for cells in CA1 (blue) and subiculum (red). We included here 56 CA1 cells and 27 subiculum cells that were stable between the two Light sessions; for neurons that were significantly directional, the two flight directions were analyzed separately (Online Methods). (**j**) Left: box-plot of remapping indices for CA1 cells (blue) and for the cell-shuffling distribution (black, representing the expected distribution for global remapping; see Online Methods); the difference was not significant (n.s.): *t*-test, $P = 0.16$. Central horizontal lines denote the medians, boxes shows the 25th and 75th percentiles and the whiskers extend to the 1st and 99th percentiles of the data. Right: full distributions for the experimental data (blue) and cell shuffling (black).

shut down in one of the modalities (**Fig. 2b**,**c** and red bars in **Fig. 2h**). Of these cells, 69% were active only under vision and 31% only under echolocation. In contrast, CA1 cells tended to be active in both modalities: only 16% (9 of 56) of the cells fired exclusively in one modality (**Fig. 2h**, blue bars). Most of the CA1 cells exhibited tuning-shape changes, i.e., shifts of place fields, that were greater than the tuning-shape changes in the subicular cells (**Fig. 2i**; *t*-test with unequal variances: $P < 0.01$). These differences between on/off remapping in the subiculum and place-field shift remapping in CA1 could not be explained by differences in firing rates, which were identical between the two areas (*t*-test comparing the peak firing rates between CA1 and subiculum cells: $P = 0.09$). Additionally, we found that the propensity of subicular neurons to undergo on/off remapping did not depend on their firing rate (*t*-test comparing the peak firing rates between the 59% of subicular neurons that underwent on/off remapping versus the 41% that did not: $P = 0.33$).

Next we compared place-field properties for those cells that were active in both conditions. We focused on 2D projections of the full 3D firing-rate maps because the 2D projections have much denser spatial coverage, allowing more robust comparisons. In particular, we compared the *xy* and *xz* projections between the vision-based and echolocation-based sessions (**Fig. 2d**–**g**). We defined a remapping index that quantified changes in tuning shape by computing 1 minus the Pearson correlation between 2D firing-rate maps for Light versus Dark ($1 - r_{2D}$); this index is high for strong remapping (**Fig. 2i**, Online Methods). The index was computed only for cells that were active in both sensory modalities (for example, those in **Fig. 2d**–**g**).

To test whether the hippocampal maps under vision and echolocation are truly orthogonal (independent), we employed the standard analysis used in rats to determine map orthogonality[29]. The empirical distribution of remapping indices was compared (separately for each anatomical region) to a cell-shuffling distribution (**Fig. 2j** and **Supplementary Fig. 6a**,**b**); for the cell shuffling, we computed remapping indices between all pairs of different cells (unrelated cells), which represents the distribution expected for global remapping[29] (Online Methods). We found that the distribution of actual remapping indices in CA1 was not significantly different from that expected from random global remapping[4] (**Fig. 2j**: *t*-test: $P = 0.16$; Kolmogorov-Smirnov test: $P = 0.39$; see also **Supplementary Fig. 6b** for similar analysis for subiculum). Note that even for totally random global remapping (**Fig. 2j**, right; black histogram), some place fields would move very little and would thus be expected to exhibit a low remapping index, as we indeed observed (**Fig. 2g**).

Finally, we examined two possible alternative interpretations of the remapping results. First, we tested whether spatial distributions of flight velocity ('velocity maps') differed between Light and Dark, which could potentially lead to shifts in place fields. However, we found that velocity maps were in fact very similar between Light and Dark (**Supplementary Fig. 6d**,**e**). We defined a velocity-change index that quantified changes in velocity maps by computing 1 minus the

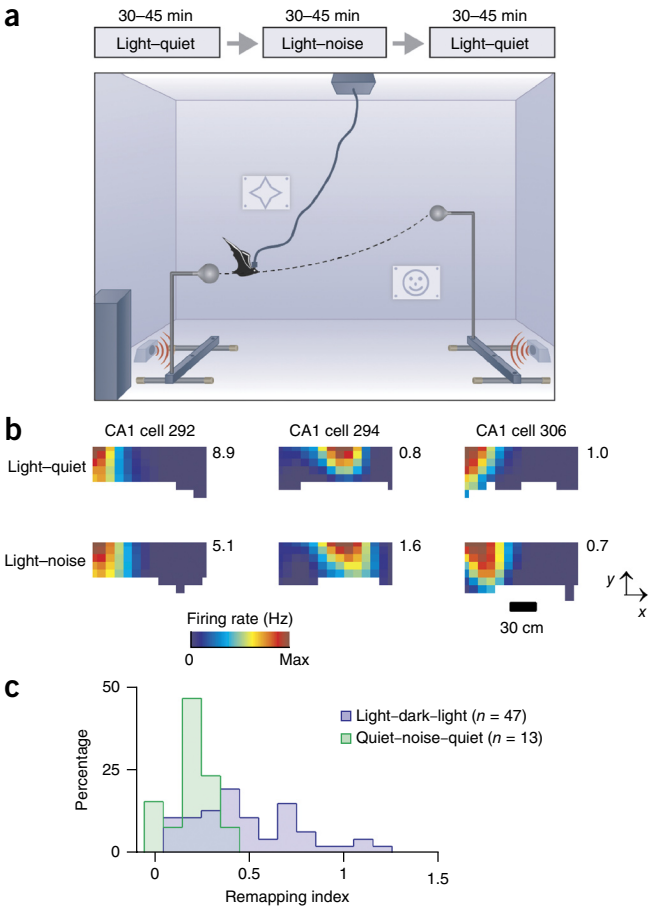

Figure 3 Place-field remapping is elicited by sensory switching from vision to echolocation and not by the masking noise. A control experiment tested whether the place-cell remapping that we observed (**Fig. 2**) might be driven by the auditory masking noise (which was not present in the dark condition), rather than by sensory differences between echolocation and vision. (**a**) Experimental design: neural data were recorded from CA1 of one bat that performed the same behavioral task as in **Figure 1a**, under a new set of conditions: session A, light without noise; session B, light with loud broadband noise. (**b**) Three example cells (columns) demonstrating similar spatial representation between the two conditions: light without noise (top row) and light with noise (bottom row). Shown are 2D firing-rate maps (*xy* projection). (**c**) The distribution of remapping indices for cells recorded in this control experiment (green, 'Quiet–noise–quiet'), compared to indices for the main experiment (blue, same as in **Fig. 2i**). The low values of the remapping index in the green histogram suggest that no remapping was elicited by the background noise alone.

Pearson correlation between 2D velocity maps for Light versus Dark; this index was close to zero for all bats (**Supplementary Fig. 6e**). Additionally, the Light–Dark velocity-change index was not correlated to the Light–Dark remapping index (**Supplementary Fig. 6e**: Pearson correlation for CA1 pyramidal cells: $r = 0.20$, $P = 0.17$). This argues against the possibility that subtle differences in velocity distributions could underlie the observed remapping. Second, we tested whether the remapping could be due not to switching from vision to sonar, but instead to the presence of the masking noise in the Light session and the absence of the noise in the Dark session, i.e., a context effect of noise *per se*, regardless of the sensory condition. To test this possibility, we trained an additional animal to perform the same behavioral task under a modified set of conditions: session A, light without noise; session B, light with noise; session A′, repeat of session A (**Fig. 3a**). We recorded 35 cells from CA1; 13 of these neurons were place cells. Individual place fields were stable between conditions A and B and did not undergo remapping (**Fig. 3b**). Across the population, no remapping was induced by the noise (**Fig. 3c**, green histogram), in striking contrast to the CA1 remapping that we found in our original experiments between Light and Dark (**Fig. 3c**, blue histogram; Kolmogorov-Smirnov test: $P < 0.0005$). We therefore conclude that the presence or absence of the noise *per se* could not explain the observed hippocampal remapping, which supports the notion that the remapping shown in **Figure 2** is purely due to the sensory differences between vision and echolocation.

In summary, the hippocampal neuronal populations that we recorded responded to the sensory switch by globally remapping. This global remapping differed systematically between CA1 and subiculum: in CA1, the cells tended to stay active under both sensory modalities, but shifted their firing fields (**Fig. 2i,j**). By contrast, cells in the subiculum tended to exhibit on/off remapping and were primarily active in one modality (**Fig. 2h**, red bars).

Spatial representation sharpens under vision versus echolocation

Egyptian fruit bat vision has an angular resolution (0.3°, ref. 15) approximately seven times sharper than the bat's echolocation-based sensory resolution (~2°, ref. 16). This difference in sensory resolutions led us to hypothesize that neuronal spatial resolution in the hippocampus may depend on the resolution of the sensory modality and to predict that place fields under vision might be smaller than place fields under echolocation[18]. To test this prediction, we compared the spatial information for hippocampal cells that were active in both vision- and echolocation-based sessions (**Fig. 4a**; Online Methods). We defined a sharpening index as the difference between spatial information in the vision session (Light) and echolocation session (Dark) divided by their sum. The distribution of sharpening indices for CA1 neurons was strongly shifted toward positive values (**Fig. 4b**), indicating that the spatial information is significantly higher (i.e., has better spatial resolution) when using vision than when using echolocation (**Fig. 4b**; *t*-test comparing to zero: main histogram, $P < 10^{-8}$; inset, $P < 10^{-8}$; sign-test: main histogram, $P < 10^{-7}$; inset, $P < 10^{-4}$). We achieved similar results using other measures to compare the compactness of CA1 place fields between vision and echolocation, such as the coherence and sparsity of firing-rate maps (**Supplementary Fig. 7a**; *t*-test, $P < 10^{-5}$ for all indices based on either spatial information, sparsity or coherence; see Online Methods). The sharpening of CA1 place fields in the Light versus the Dark could not be explained by differences in place-field stability, because the stability was not significantly different between the two sensory conditions (**Supplementary Fig. 7c**; paired *t*-test, $P = 0.12$). Some subiculum cells also showed substantial place-field sharpening (**Fig. 4a**, cell 102), but across the subicular population the sharpening effect was much weaker than in CA1, although it was marginally significant (**Fig. 4c**; paired *t*-test: main histogram, $P = 0.0476$; inset, $P = 0.0481$; **Supplementary Fig. 7b**, when using coherence: $P = 0.029$; **Fig. 4c**: sign-test for both main and inset: $P = 0.45$; note however that the number of subicular neurons active in both sessions was rather small). We did not find any significant correlation between the remapping index and the sharpening index (CA1: $r = 0.21$, $P = 0.20$; subiculum: $r = 0.03$, $P = 0.93$), which suggests that remapping and sharpening are two largely independent phenomena. Overall, these results support the hypothesis[18] that vision-based place fields are indeed sharper and more compact than echolocation-based place fields.

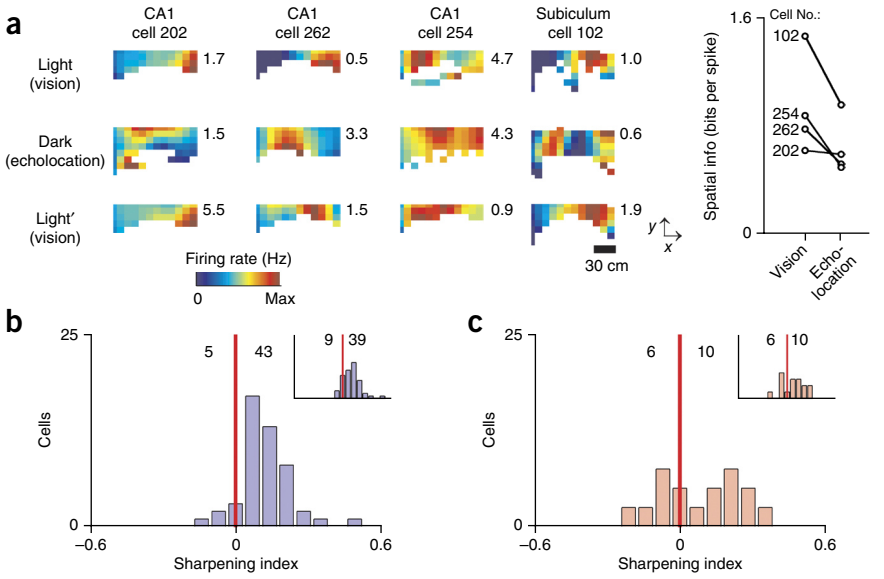

Figure 4 Spatial representation sharpens under vision versus echolocation. (**a**) Four example cells (columns) demonstrating a sharper representation in vision-based sessions as compared to the echolocation-based session; shown are 2D firing-rate maps (*xy* projection) for the three behavioral sessions (vision–echolocation–vision′). Right plot: spatial information under vision (averaged over both Light sessions) versus echolocation, for the four example cells on the left. (**b**) Distribution of sharpening index, calculated as $(I_{vision} - I_{echolocation})/(I_{vision} + I_{echolocation})$ (see Online Methods) for the CA1 place cells, showing spatial information computed over all pixels available for each session; numbers indicate numbers of cells with sharpening indexes above or below 0 (marked by red line). Inset: spatial information using only the region that overlapped behaviorally between the sessions (Online Methods). Axes are identical in main graph and inset. (**c**) Distribution of sharpening index for subiculum place cells. As in **b**, axes are identical in main graph and inset. Note the rightward shift of the histograms, indicating a strong sharpening effect in CA1 (**b**) and weak sharpening in subiculum (**c**).

We also tested the theoretical effect of sensory resolution on spatial resolution in several commonly used models of place cells: the continuous-attractor model, boundary vector-cell model and view-based model[30–35]. We simulated these models and degraded the sensory resolution of the input in each model, and computationally tested the effect of this sensory degradation on the spatial tuning of simulated place cells. These simulations suggested that the spatial sharpening effect is best explained by combining sensory-based and path-integration mechanisms (**Supplementary Figs. 8** and **9**).

Interneurons exhibit remapping and sharpening phenomena similar to those of pyramidal cells

To examine possible remapping in hippocampal interneurons, we recorded 34 interneurons from CA1 (**Fig. 1c**; Online Methods) and conducted similar analyses to those described above for the pyramidal cells. First, we found that although the spatial tuning of interneurons was very broad (**Fig. 5a**), almost all interneurons nevertheless carried significant spatial information (31 of 34 interneurons, based on a 95% shuffling criterion for the spatial information; see Online Methods), like interneurons in rat CA1 (ref. 36). Additionally, almost all of the bat interneurons exhibited directional tuning (29 of 34 cells; see **Supplementary Fig. 10**).

Second, in the Light–Dark–Light′ experiment, we found that many interneurons responded to the sensory modality change (**Fig. 5a**). We analyzed 43 interneurons, which were included here on the basis of stability criteria and separated into the two flight directions (Online Methods). All interneurons were active in both conditions, but many of them changed their spatial tuning in the echolocation-based condition, reverting to the original tuning in the second vision-based session (**Fig. 5a**). We repeated the same remapping analyses as we used for pyramidal cells, revealing that the remapping-index distribution for interneurons was not significantly different from that expected from global remapping (**Fig. 5b** and **Supplementary Fig. 6c**; *t*-test: $P = 0.43$; Kolmogorov-Smirnov test of experimental data versus cell-shuffling distribution: $P = 0.32$). To our knowledge, this is the first demonstration that remapping in hippocampal interneurons can involve changes in the shape of the (broad) spatial tuning of the interneurons.

Finally, the spatial resolution of interneurons changed between vision and echolocation conditions, like that of the CA1 pyramidal population (**Fig. 5c**; compare to **Fig. 4b**): the distribution of sharpening indices was significantly shifted to positive values, indicating that for most interneurons, vision-based spatial information was greater than echolocation-based spatial information (**Fig. 5c**; *t*-test versus 0: main histogram, $P < 10^{-10}$; inset, $P < 10^{-9}$). This surprising finding further corroborates our results from pyramidal cells and demonstrates that vision-based hippocampal maps for both place cells and interneurons are sharper and more compact than echolocation-based maps. More generally, this supports the hypothesis that the resolution of the sensory input strongly influences the spatial resolution of the hippocampal map[18].

DISCUSSION

Here we demonstrate that sensory differences can drive global remapping in the mammalian hippocampus, i.e., a switch between completely different spatial maps. Specifically, we found that switching between sensory modalities elicited strong remapping in the bat hippocampus, although both modalities, vision and echolocation, were tested in the same identical physical environment and in the same behavioral task (ball-to-ball flights). Thus, the same space was represented differently under the two sensory conditions. Furthermore, CA1 and subiculum cells differed dramatically in their remapping properties: CA1 cells tended to shift their firing fields, while subiculum cells tended to shut off in one of the sensory modalities. Interestingly, the spatial maps for the two modalities differed in their spatial-coding resolution, suggesting that sensory resolution determines spatial resolution[18]. This latter result was used to test the predictions of different theoretical models of place cells. Results of this analysis indicated that a hybrid model combining sensory inputs and path-integration may best describe the sharpening data. Finally, we found that, like pyramidal cells, hippocampal interneurons exhibited sharpening of their (broad) spatial tuning when tested under vision versus echolocation and also exhibited strong global remapping between the two sensory conditions.

Our results seem to be in contrast to those of some rodent studies, which reported similar spatial maps under light and dark conditions[12]. This could be explained in several ways. First, there could be species

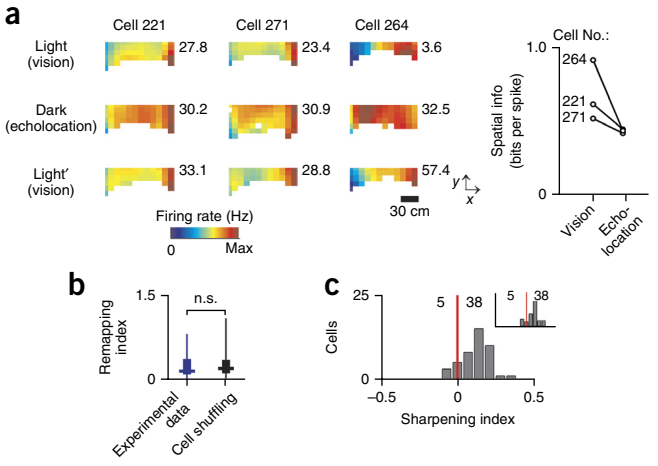

Figure 5 Most CA1 interneurons exhibit remapping and sharpening of their spatial maps under vision versus echolocation. (**a**) Examples of three interneurons (columns) demonstrating remapping between sensory conditions (rows), as well as sharper spatial representation in vision versus echolocation. Plotted as in **Figure 4a**. Right plot: spatial information under vision (averaged over both Light sessions) versus echolocation, for the three example cells on the left. (**b**,**c**) Population analyses. We included here 43 CA1 interneurons that were stable between the two Light sessions; for neurons that were significantly directional, the two flight directions were analyzed separately (Online Methods). (**b**) Remapping indices for interneurons were not significantly different from a cell-shuffling distribution (global remapping) (*t*-test: $P = 0.43$). Box plot: same graphical conventions as in **Figure 2j**. See **Supplementary Figure 6c** for the full distributions. (**c**) Distribution of sharpening index, plotted as in **Figure 4b**; the distribution is strongly shifted to the right, suggesting that the higher sensory resolution under vision results in a sharper spatial representation in interneurons as well.

differences in remapping dynamics between bats and rats. Second, most previous studies in rats had a restricted ability to control for proximal olfactory and somatosensory (whisking-based) cues. These proximal cues may be highly informative for rodents and thus might generate a similar spatial map for both conditions. In our experiments, we used ventilators to blow away odor trails from mid-air, and this cleaner sensory dissociation could underlie the strong global remapping (orthogonalization) that we found in the bat, as compared to previous rodent studies that showed either no remapping or very mild remapping[12,13].

We observed in CA1 interneurons the same basic phenomena that we found in pyramidal cells: strong remapping and sharpening of spatial representations. Changes of interneuron firing rates have been previously reported during exploration of novel environments[3,36,37], and a few studies have linked the changes in interneuron firing rates to the formation of a new pyramidal cell spatial maps following learning[3,38]. To our knowledge, our results are the first to show that interneurons maintain multiple spatial representations that can switch in a context-dependent manner, akin to the global remapping phenomenon in pyramidal cells.

The striking difference in the remapping properties between the bat's subiculum and its CA1, whereby the subicular network exhibited a dramatic on/off type of global remapping, similar to that in CA3 (ref. 4), raises the question of what the subiculum is good for. The function of the subiculum within the hippocampal circuit is unclear. Considering that the subiculum is almost as strongly recurrent as CA3 (refs. 39,40) and that the subiculum sends massive projections outside of the hippocampus[40], we suggest that the subiculum is in fact a key region conferring strong nonlinear dynamical processing capabilities, which contribute to making the hippocampus the powerful memory and navigation system that it is (see further details and explanations in **Supplementary Fig. 11a**).

Finally, the remapping results we report in this study may suggest the existence of separate maps for every different condition under which the environment is experienced[41,42]. Imagine the following analogy: when a human navigates through a landscape during nighttime, the most salient landmarks would be the lights of towns and factories, while the same landscape during daytime will yield other landmarks, such as mountain ranges and agricultural fields. This could result in different maps of the same space for day versus night[18] (see discussion in **Supplementary Fig. 11b**). This does not necessarily mean that there are an infinite number of maps for each environment, because the number of such distinct conditions is in fact rather limited. Instead, we propose a 'cognitive atlas' hypothesis: we posit that the same environment is represented by a small set of different maps for different conditions, akin to a world atlas that contains multiple maps for the same space, such as a physical map, political map, road map, land use map, etc. We differentiate the notion of the cognitive atlas from similar notions such as the 'multiple charts'[43] and 'multiple maps' hypotheses[41], both of which refer primarily to remapping between different environments, different reference frames, or different behaviors. By contrast, in our experiments, echolocation and vision sessions were performed in the same environment, with the same behavioral task, and animals exhibited the same flight trajectories, but the hippocampus exhibited global remapping. Therefore, to emphasize the existence of completely different (orthogonal) maps for the same space and same behavioral task, we termed this set of maps a cognitive atlas. It is unclear where the binding or the alignment (co-registration) of the maps in this cognitive atlas could take place. One possibility is that it occurs outside of the hippocampus—for example, in the medial entorhinal cortex. Another option is that there might be a population of 'abstract map' cells in the hippocampus itself, which encodes space irrespective of the sensory condition (see **Supplementary Fig. 11b** and **Fig. 2g**). However, the orthogonal nature of the remapping (**Fig. 2h–j**) speaks strongly against the existence of such truly stable cells and suggests that, in fact, all the cells in the hippocampus remap between the two sensory conditions. Taken together, our results are not consistent with the notion that the hippocampus contains an abstract map of space; instead, the data are consistent with the notion of multiple use-dependent maps representing the same space: a cognitive atlas.

METHODS

Methods and any associated references are available in the online version of the paper.

Note: Any Supplementary Information and Source Data files are available in the online version of the paper.

ACKNOWLEDGMENTS

We thank A. Treves, D. Derdikman, A. Finkelstein, A. Rubin, G. Ginosar, A. Sarel, D. Omer and M. Tsodyks for discussions and comments on the manuscript; S. Kaufman for bat training and assistance in neural recordings; J.-M. Fellous, S. Weiss and O. Gobi for help in experiments; B. Pasmantirer, G. Ankaoua and L. Goffer for mechanical designs; A. Averkin for help in camera calibrations for 3D tracking; A. Tuval and M. Weinberg for veterinary support; G. Brodsky for graphics; D. Sheynikhovich for simulations of the view-based model; C. Ra'anan and R. Eilam for histology; and M.P. Witter for discussions and advice on histological delineations of CA1 and subiculum. This study was supported by research grants to N.U. from the European Research Council (ERC – NEUROBAT), the Human Frontiers Science Program (HFSP RGP0062/2009-C), the Israel Science Foundation (ISF 1017/08 and ISF 1319/13) and the Minerva Foundation. S.R. was supported by the Howard Hughes Medical Institute.

AUTHOR CONTRIBUTIONS

M.G.-S. and N.U. designed the experiments, with inputs from L.L. Experiments were conducted by M.G.-S., with contributions of L.L. to some of the surgeries and tetrode recordings. M.G-S. analyzed the data and discussed the results and interpretations with L.L. and N.U. M.G.-S. and S.R. carried out model simulations and wrote the corresponding methods section. M.G.-S. and N.U. wrote the manuscript, with major inputs from L.L.; S.R. commented on the manuscript.

COMPETING FINANCIAL INTERESTS

The authors declare no competing financial interests.

1. O'Keefe, J. & Nadel, L. *The Hippocampus as a Cognitive Map* (Oxford University Press, 1978).
2. Eichenbaum, H. & Cohen, N.J. Can we reconcile the declarative memory and spatial navigation views on hippocampal function? *Neuron* **83**, 764–770 (2014).
3. Wilson, M.A. & McNaughton, B.L. Dynamics of the hippocampal ensemble code for space. *Science* **261**, 1055–1058 (1993).
4. Leutgeb, S., Leutgeb, J.K., Treves, A., Moser, M.-B. & Moser, E.I. Distinct ensemble codes in hippocampal areas CA3 and CA1. *Science* **305**, 1295–1298 (2004).
5. McHugh, T.J., Blum, K.I., Tsien, J.Z., Tonegawa, S. & Wilson, M.A. Impaired hippocampal representation of space in CA1-specific NMDAR1 knockout mice. *Cell* **87**, 1339–1349 (1996).
6. Ono, T., Nakamura, K., Nishijo, H. & Eifuku, S. Monkey hippocampal neurons related to spatial and nonspatial functions. *J. Neurophysiol.* **70**, 1516–1529 (1993).
7. Ekstrom, A.D. *et al.* Cellular networks underlying human spatial navigation. *Nature* **425**, 184–188 (2003).
8. Ulanovsky, N. & Moss, C.F. Hippocampal cellular and network activity in freely moving echolocating bats. *Nat. Neurosci.* **10**, 224–233 (2007).
9. Ulanovsky, N. & Moss, C.F. Dynamics of hippocampal spatial representation in echolocating bats. *Hippocampus* **21**, 150–161 (2011).
10. Yartsev, M.M., Witter, M.P. & Ulanovsky, N. Grid cells without theta oscillations in the entorhinal cortex of bats. *Nature* **479**, 103–107 (2011).
11. Yartsev, M.M. & Ulanovsky, N. Representation of three-dimensional space in the hippocampus of flying bats. *Science* **340**, 367–372 (2013).
12. Quirk, G.J., Muller, R.U. & Kubie, J.L. The firing of hippocampal place cells in the dark depends on the rat's recent experience. *J. Neurosci.* **10**, 2008–2017 (1990).
13. Markus, E.J., Barnes, C.A., McNaughton, B.L., Gladden, V.L. & Skaggs, W.E. Spatial information content and reliability of hippocampal CA1 neurons: effects of visual input. *Hippocampus* **4**, 410–421 (1994).
14. Save, E., Nerad, L. & Poucet, B. Contribution of multiple sensory information to place field stability in hippocampal place cells. *Hippocampus* **10**, 64–76 (2000).
15. Heffner, R.S., Koay, G. & Heffner, H.E. Sound localization in an Old-World fruit bat (*Rousettus aegyptiacus*): acuity, use of binaural cues, and relationship to vision. *J. Comp. Psychol.* **113**, 297–306 (1999).
16. Yovel, Y., Falk, B., Moss, C.F. & Ulanovsky, N. Optimal localization by pointing off axis. *Science* **327**, 701–704 (2010).
17. Yovel, Y., Geva-Sagiv, M. & Ulanovsky, N. Click-based echolocation in bats: not so primitive after all. *J. Comp. Physiol. A Neuroethol. Sens. Neural Behav. Physiol.* **197**, 515–530 (2011).
18. Geva-Sagiv, M., Las, L., Yovel, Y. & Ulanovsky, N. Spatial cognition in bats and rats: from sensory acquisition to multiscale maps and navigation. *Nat. Rev. Neurosci.* **16**, 94–108 (2015).
19. Danilovich, S. *et al.* Bats regulate biosonar based on the availability of visual information. *Curr. Biol.* **25**, R1124–R1125 (2015).
20. Sharp, P.E. & Green, C. Spatial correlates of firing patterns of single cells in the subiculum of the freely moving rat. *J. Neurosci.* **14**, 2339–2356 (1994).
21. Kim, S.M., Ganguli, S. & Frank, L.M. Spatial information outflow from the hippocampal circuit: distributed spatial coding and phase precession in the subiculum. *J. Neurosci.* **32**, 11539–11558 (2012).
22. Csicsvari, J., Hirase, H., Czurko, A. & Buzsáki, G. Reliability and state dependence of pyramidal cell-interneuron synapses in the hippocampus: an ensemble approach in the behaving rat. *Neuron* **21**, 179–189 (1998).
23. Kjelstrup, K.B. *et al.* Finite scale of spatial representation in the hippocampus. *Science* **321**, 140–143 (2008).
24. Rubin, A., Yartsev, M.M. & Ulanovsky, N. Encoding of head direction by hippocampal place cells in bats. *J. Neurosci.* **34**, 1067–1080 (2014).
25. McNaughton, B.L., Barnes, C.A. & O'Keefe, J. The contributions of position, direction, and velocity to single unit activity in the hippocampus of freely-moving rats. *Exp. Brain Res.* **52**, 41–49 (1983).
26. Hollup, S.A., Molden, S., Donnett, J.G., Moser, M.-B. & Moser, E.I. Accumulation of hippocampal place fields at the goal location in an annular watermaze task. *J. Neurosci.* **21**, 1635–1644 (2001).
27. Ravassard, P. *et al.* Multisensory control of hippocampal spatiotemporal selectivity. *Science* **340**, 1342–1346 (2013).
28. Boonman, A., Bar-On, Y., Cvikel, N. & Yovel, Y. It's not black or white-on the range of vision and echolocation in echolocating bats. *Front. Physiol.* **4**, 248 (2013).
29. Fyhn, M., Hafting, T., Treves, A., Moser, M.-B. & Moser, E.I. Hippocampal remapping and grid realignment in entorhinal cortex. *Nature* **446**, 190–194 (2007).
30. Hartley, T., Burgess, N., Lever, C., Cacucci, F. & O'Keefe, J. Modeling place fields in terms of the cortical inputs to the hippocampus. *Hippocampus* **10**, 369–379 (2000).
31. Sheynikhovich, D., Chavarriaga, R., Strösslin, T., Arleo, A. & Gerstner, W. Is there a geometric module for spatial orientation? Insights from a rodent navigation model. *Psychol. Rev.* **116**, 540–566 (2009).
32. Romani, S. & Tsodyks, M. Short-term plasticity based network model of place cells dynamics. *Hippocampus* **25**, 94–105 (2015).
33. Barry, C. *et al.* The boundary vector cell model of place cell firing and spatial memory. *Rev. Neurosci.* **17**, 71–97 (2006).
34. Strösslin, T., Sheynikhovich, D., Chavarriaga, R. & Gerstner, W. Robust self-localisation and navigation based on hippocampal place cells. *Neural Netw.* **18**, 1125–1140 (2005).
35. McNaughton, B.L., Battaglia, F.P., Jensen, O., Moser, E.I. & Moser, M.-B. Path integration and the neural basis of the 'cognitive map'. *Nat. Rev. Neurosci.* **7**, 663–678 (2006).
36. Nitz, D. & McNaughton, B. Differential modulation of CA1 and dentate gyrus interneurons during exploration of novel environments. *J. Neurophysiol.* **91**, 863–872 (2004).
37. Frank, L.M., Stanley, G.B. & Brown, E.N. Hippocampal plasticity across multiple days of exposure to novel environments. *J. Neurosci.* **24**, 7681–7689 (2004).
38. Dupret, D., O'Neill, J. & Csicsvari, J. Dynamic reconfiguration of hippocampal interneuron circuits during spatial learning. *Neuron* **78**, 166–180 (2013).
39. Harris, E., Witter, M.P., Weinstein, G. & Stewart, M. Intrinsic connectivity of the rat subiculum: I. Dendritic morphology and patterns of axonal arborization by pyramidal neurons. *J. Comp. Neurol.* **435**, 490–505 (2001).
40. Amaral, D. & Lavenex, P. in *The Hippocampus Book* (eds. Andersen, P., Morris, R.G., Amaral, D.G., Bliss, T.V. & O'Keefe, J.) 37–115 (Oxford University Press, 2007).
41. Redish, A.D. *Beyond the Cognitive Map: From Place Cells to Episodic Memory* (MIT Press, 1999).
42. Wood, E.R., Dudchenko, P.A., Robitsek, R.J. & Eichenbaum, H. Hippocampal neurons encode information about different types of memory episodes occurring in the same location. *Neuron* **27**, 623–633 (2000).
43. Samsonovich, A. & McNaughton, B.L. Path integration and cognitive mapping in a continuous attractor neural network model. *J. Neurosci.* **17**, 5900–5920 (1997).

ONLINE METHODS

Subjects. We implanted 7 adult male Egyptian fruit bats (*Rousettus aegyptiacus*, weight 163–174 g at implantation) with tetrodes aimed at the dorsal CA1 area of the hippocampus ($n = 4$) or subiculum ($n = 3$). Six of these animals (3 with CA1 implants and 3 with subiculum implants) were tested with a full set of behavioral sessions, as described below, and their data were used for all the analyses in this study; the seventh animal was tested daily in a single flight-session and its data were used only for directionality analyses (**Fig. 1e** and **Supplementary Fig. 2**; see below). An additional, eighth animal with a CA1 implant was tested under a different set of conditions (see **Fig. 3**). All experimental procedures were approved by the Institutional Animal Care and Use Committee of the Weizmann Institute of Science.

Behavioral task, training and recording environment. Bats were trained to fly back and forth along a 1.5-m linear flyway embedded in a three-dimensional (3D) room (2.5 × 1.7 × 2.5 m), in order to obtain food that was placed on a large polystyrene target ball (10 cm in diameter) mounted on a vertical pole. A target ball was positioned at both ends of the flyway. After every flight lap (flight with successful landing), the target was randomly repositioned between one of 9 possible options: 3 horizontal positions in the y axis × 3 vertical positions in the z axis (**Fig. 1a**); this ensured a variety of goal-directed 3D trajectories across different flights.

Vision-based sessions. The bats learned to perform this task in a lit room (illuminance: 2 lux), which included many visual landmarks, such as multiple objects within the room and visual cues on the walls (**Fig. 2a**, left). To ensure that bats were using purely vision in this condition, we undertook several measures. (i) To prevent the use of echolocation, broadband noise (5–120 kHz; intensity 85 dB SPL) was played from two speakers (ultrasonic dynamic speaker ScanSpeak; Avisoft Bioacoustics; frequency range 1–120 kHz) located at both ends of the room, facing the bat's flight direction (**Fig. 2a**, left). (ii) To blow away odor cues from mid-air, two ventilators were placed on the two sides of the flyway. (iii) Randomization of target location after each lap ensured that bats could not rely on procedural motor memory.

Echolocation-based sessions. The walls and ceiling of the room were covered with acoustic foam and the pole was covered with felt, to minimize reverberations; in contrast, the target sphere was made of an acoustically highly reflective material (polystyrene), in order to make it the most salient acoustically reflective object in the flight room. Additionally, the room contained multiple salient objects that served as both visual and echo-reflecting landmarks (for example, the cabinet, speakers, cameras, microphones and cable commutator box hanging from the ceiling: see **Figs. 1a** and **2a**). The room also contained paper-printed visual landmarks that were hung on the foam that covered the walls (for example, the smiley plotted in **Fig. 2a**); note that such paper sheets could also serve as acoustic landmarks in darkness, because paper is much more acoustically reflective at ultrasonic frequencies than the surrounding sound-absorbing foam. We took several measures to ensure that the bats were relying solely on echolocation to perform the task in the dark. (i) To exclude use of visual cues, the target was painted black and the room was in complete darkness (illuminance: 10^{-6} lux; bats were tracked via infrared LEDs; the experimenter, who was inside the room, used night-vision goggles with infrared illumination). (ii) As in the light session, we installed ventilators to remove possible mid-air odor trials. (iii) Target position was randomized, as in the light session.

Pretraining and training. Stage 1: in the first 5–10 d, the bats were pretrained and learned to fly between the balls in a lit environment in the absence of a broadcasted noise. This was done in the same experimental room where neural recordings later took place, which ensured that the bats had 5–10 d to perceive this space using both vision and echolocation and thus to understand the layout of this space using either sensory system. Stage 2: After learning the basic paradigm, the training was split to two flight rooms for additional 5–10 d: in the smaller room (where recording eventually took place), the bats performed the task in the light with broadcast noise; and in the larger room, they performed it in complete darkness. Subsequently, bats were implanted with a tetrode microdrive (see below). Stage 3: Neural recordings started after the bats recovered from surgery and were able to fly >100 laps per session, and once tetrodes reached the hippocampal pyramidal cell layer. At that time, the bats were introduced for the first time to the experimental room (small flight room) in complete darkness. Subsequently, we recorded the neural activity during three behavioral sessions per day (A–B–A′ design): (i) vision (light condition); (ii) echolocation (dark condition); (iii) a repetition of the vision (light) condition. The duration of each behavioral session was typically 30–45 min. Each behavioral session was flanked by rest sessions, which lasted ~20 min per session. During these sessions, the bat was placed in a small cage positioned inside the experimental room (in the middle of the behavioral region), where it could hang and rest. The cage allowed the bat to watch the room's interior. In some rest sessions we tracked the bat's movements within the cage: these data demonstrated that the animals were wide awake during these rest sessions and often exhibited substantial movements in the cage, including around the time of the sensory switch (see **Supplementary Fig. 5e**). Throughout the duration of the daily experiment (3 behavioral sessions + 4 rest sessions), the bats were not taken outside the recording room, and the neural recordings were done continuously without disconnecting the recording cable (see below more information on recording methods).

Behavioral controls between vision- and echolocation-based sessions. The spatial coverage of the flights was very similar between the vision- and echolocation-based sessions (**Supplementary Fig. 5b,c**; paired t-test comparing spatial coverage in light versus dark for implanted bats which had more than 4 recording days: $P > 0.1$ for all bats; see below section "Analysis of behavioral coverage" for further details). The velocity differences between the light and dark conditions were very small: 2%, 3% and 6% mean velocity difference for bats No. 9343, 6255 and 9673, respectively; see **Supplementary Fig. 5b** (although these small differences were significant for 2 of the 3 bats: paired t-test for the 3 bats: $P = 0.02$, $P = 0.003$ and $P = 0.23$, respectively). These small but significant velocity differences did not cause any significant differences between light and dark mean firing rates (t-test for mean firing rates: CA1 pyramidal cells, $P = 0.29$; subiculum pyramidal cells, $P = 0.39$; CA1 interneurons, $P = 0.23$). Finally, we conducted a separate behavioral experiment where we checked whether bats ($n = 3$) could find their way to the target ball in the dark while we played the broadband noise. This 'dark + noise' manipulation caused a dramatic drop in behavioral performance compared to the standard sessions (**Supplementary Fig. 5a**; paired t-test comparing performance in control versus dark + noise sessions: $P < 10^{-7}$), which confirmed the effectiveness of the broadband noise and emphasized the clean double dissociation between using vision in the light sessions and using echolocation in the dark session.

Two steps were taken in order to ensure that the bats recognized the fixed identity of the experimental room. First, all the bats in this study were initially pre-trained without any echolocation-masking noise for 5–10 d in the same room in which the recording later took place; during this initial pre-training both visual and echolocation cues were available simultaneously and thus they learned this space using both senses. Second, during each recording day the bats were connected continuously to the recording cable and were never taken out of the room between the behavioral sessions.

In one of the subiculum bats, the vision sessions were conducted without broadcasting broadband noise. Because Egyptian fruit bats dramatically lower their echolocation click rate at the light levels that we used[19], we pooled the neurons of this single bat with the other subiculum bats.

Video recordings. The bat's positions were recorded using two video trackers, connected to two infrared cameras placed at two of the upper corners of the flight-room. These cameras tracked the position of two infrared light-emitting diodes (LEDs) connected to the head-stage on the bat's head in both light and dark conditions; the same infrared-LEDs were used for video tracking during both the light and the dark sessions. Positional data were collected and stored at a 25-Hz sampling rate. The bat's 3D position in the flight room was reconstructed using the direct linear transform algorithm, applied to the data from the two cameras, similar to the method described previously[11,16]. We included in the analysis only valid video frames for which video data were available from both cameras (i.e., the bat was within the field of view of both cameras, with no occlusions from either camera). If segments of video data were missing, we interpolated the video data using cubic spline; interpolation was done only up to 160 ms from the last valid video frame. We verified that cubic spline interpolation faithfully followed the bat's trajectory over such short time periods (160 ms). 3D locations within the flight room were calibrated using 81 calibration points that spanned the volume of the room; this large number of calibration points allowed achieving a mean positional reconstruction accuracy of 8 mm across the room. Reconstruction accuracy was estimated using a leave-one-out algorithm, in which every point was

reconstructed based on the remaining 80 calibration points. Additional calibrations were conducted at least once a week to validate the stability of the cameras and ensure that the reconstruction accuracy of 3D positions was maintained throughout the recordings.

Surgery and electrophysiological recording. All surgical procedures were as described previously[8,10,11]. Briefly, after completion of training, bats were implanted with a four-tetrode microdrive (weight 2.1 g; Neuralynx), loaded with tetrodes constructed from four strands of insulated 17.8-μm platinum–iridium wire. Tetrodes were gold-plated to reduce wire impedance to 0.3–0.7 M (at 1 kHz). The microdrive was implanted above the right dorsal CA1 (3.75 mm lateral to the midline and 5.8 mm anterior to the transverse sinus that runs between the posterior part of the cortex and the cerebellum), or above the right subiculum (3.1 mm lateral to midline and 4.9 mm anterior to the transverse sinus). Following surgery, the tetrodes were slowly lowered toward the CA1 or subiculum pyramidal layer; positioning of tetrodes in the layer was provisionally determined by the presence of high-frequency field oscillations ('ripples') and associated neuronal firing and was later verified histologically[10,11]. For each bat, one tetrode was left in an electrically quiet zone and served as a reference, and the remaining three tetrodes served as recording probes. During recordings, a unity-gain preamplifier (HS-18; Neuralynx) was attached to a connector on the microdrive through a thin and flexible tether cable (Litz cable, 2.5 m long; Neuralynx), which allowed bats to fly freely along the designated linear flyway. This lightweight cable did not restrict the bats' flight, and they easily performed >100 flight laps in each behavioral session (>300 laps daily). Signals were amplified (1,400–5,000×) and bandpass filtered (600–6,000 Hz; Digital Lynx, Neuralynx), and a voltage threshold was used for collecting 1-ms spike waveforms sampled at 32 kHz. In one of the animals, data were collected using a wireless electrophysiology recording system (a modified version of the wireless device used in ref. 11). To reduce the likelihood of duplicate recordings of the same cell in more than one session, tetrodes were moved after each recording day.

Spike sorting. All spike-sorting procedures were identical to those described previously[8,10]. Briefly, spike waveforms were sorted on the basis of their relative energies and amplitudes on different channels of each tetrode (SpikeSort3D; Neuralynx). Well-isolated clusters of spikes were manually encircled ('cluster cutting'), and a refractory period (2 ms) in the interspike interval histogram was verified. We used a standard measure of cluster isolation quality which is commonly used in rats, the isolation distance index[11,44]. This index calculates the distances between spike clusters of different cells in Mahalanobis space using principal components and spike-energy features[44]. There was no significant difference between the isolation indices of CA1 cells and subiculum cells (the mean isolation distances were 95.5 and 92.1 for CA1 and subiculum cells respectively; *t*-test: $P = 0.72$).

Putative pyramidal cells were identified based on the following: (1) spike waveform followed by long after-hyperpolarization; (2) mean firing rate < 5 Hz; (3) interspike interval histograms indicating complex-spike bursts; and (4) the simultaneous recording of other complex-spike cells[8,10]. Putative interneurons were identified as follows[22]: (1) narrow spike waveform (0.2 ms); (2) mean firing rate > 5 Hz (see **Fig. 1c**, bottom-right quadrant). This yielded a total of 84 and 107 pyramidal cells in CA1 and subiculum, respectively; of these, 59 and 48 pyramidal cells, respectively, were behaviorally active (more than 25 spikes per session in at least one session, with spikes distributed over at least 5 flights and peak firing rate > 0.5 Hz; note that many neurons had much higher peak rates of >5 Hz: see **Supplementary Fig. 5d**). Additionally, we recorded 34 interneurons in CA1 (and 1 in subiculum; this one subicular interneuron was not used for analysis).

Neurons were classified as place cells based on a shuffling procedure on the spatial information[10], if the neuron passed the 95th shuffling percentile in at least one of the two flight directions (Online Methods): 90% (53/59) of the behaviorally active pyramidal cells in CA1 were classified as place cells, and 85% (41/48) of the behaviorally active pyramidal cells in the subiculum were classified as place cells. These percentages were rather similar to those reported in CA1 and subiculum of rats running on long linear tracks[21,23] and in two-dimensional arenas[3,20]. We assessed the stability of the place fields by partitioning each session into even and odd minutes and calculating the Pearson correlation coefficient between the 2D *xy*-projection firing-rate maps computed for odd versus even minutes (**Supplementary Figs. 1** and **7c**,**d**).

Computing firing-rate maps. Firing-rate maps were constructed for flight periods only. Individual flights were identified as time epochs during which the bat's 3D velocity was higher than 20 cm/s. To improve the accuracy in estimating flight velocity, the bat's position was smoothed using a smoothing spline (*csaps.m* in Matlab), based on which the instantaneous velocity was extracted. Further, to ensure that takeoff and landing data did not contaminate the pure flight epochs, we removed from analysis the vicinity of the landing balls (approximately 10 cm at each end). Flight epochs were classified automatically as described above, and subsequently all flights were manually inspected in order to ensure that only valid unidirectional trajectories were included in the data set.

All the analyses and statistical tests in this study were performed strictly on the basis of 2D firing-rate maps with fixed pixels. To compute 2D projections of the firing fields, we used fixed-sized pixels (10×10 cm^2) and collapsed the time-spent (occupancy) data and the spike counts onto the relevant 2D dimension (*xy*, *xz* or *yz*). We smoothed both the spike-count and time-spent 2D maps with a Gaussian kernel ($\sigma = 1.5$ bins), and then divided, bin by bin, the smoothed 2D spike-count by the smoothed 2D time spent. Bins (2D pixels) in which the bat spent <150 ms during the session were excluded from the 2D firing-rate map and were colored white. We did not apply any adaptive smoothing to the 2D firing-rate maps.

We computed also 3D firing-rate maps for display purposes only; these were used only for plotting **Supplementary Figure 2a**,**b** (row 2). For these 3D firing-rate maps, the 3D volume of the room was partitioned into $10 \times 10 \times 10$ cm^3 voxels, and we calculated the number of spikes in each bin divided by the time spent in it, using an adaptive smoothing algorithm (see ref. 11 for details). These 3D firing-rate maps were used here for visualization only; all the analyses and statistics were done on the projected 2D maps with fixed bin sizes (without adaptive smoothing).

Analysis of behavioral coverage. For each behavioral session, we computed the radius of space that was covered by the back-and-forth flights: this radius was computed in the middle of the flyway. We found no significant difference between 3D light versus dark coverage for the bats that we analyzed (**Supplementary Fig. 5b**,**c**). A different analysis, comparing the number of 2D pixels covered in 2D projections (*xy*, *xz*, *yz*), found no significant differences between light sessions and dark sessions in the *xz* and *yz* projections, but in the *xy* projection there was a slight enlargement of the number of voxels covered in the dark session. We addressed this issue by conducting additional analysis of firing-rate maps based only on the voxels that overlapped in their coverage between light and dark (see below; and c.f. **Figure 4b**,**c** insets).

Definition of place cells. We used a shuffling procedure on the spatial information (see below) to determine if a recorded neuron was a place cell, by comparing the empirical value of the spatial information for each cell to the confidence interval of a spike-shuffled distribution. The shuffled distribution was generated by randomly shifting in a rigid manner the timestamps of the cell's spike train, while making sure that shuffled spikes would occur only during valid flight periods. This shuffling procedure was repeated 1,000 times for each neuron. For each repetition, the 2D firing-rate maps were generated anew in the same manner as described above, and the spatial information was recomputed. Active neurons for which the empirical values of spatial information exceeded the upper 95% confidence interval of their shuffled distribution were defined as significant place cells.

Additionally, we examined the within-session stability of place fields, by computing the Pearson correlation between odd and even minutes of each session (**Supplementary Fig. 1**). The stability of place cells was found to be extremely high, with mean $r = 0.80$ (see **Supplementary Fig. 1b**).

Directionality of firing. We used two different measures to determine whether the activity of a cell differed between flight directions. (i) Place-field shape change: 2D firing-rate maps were constructed for the neural activity separately for each flight direction, and we computed the Pearson correlations between 2D projections for the two directions, using only those 2D pixels that were sampled in both flight directions. (ii) Firing-rate change: for each session, a contrast index was calculated as the absolute difference of the average firing rates in both flight directions, divided by their sum. We then applied a shuffle-based significance test to determine which cells were directionally tuned. For every recording session we randomly assigned a flight direction for each flight, keeping the original percentage of the two flight directions; the 2D firing-rate maps were then recomputed as

doi:10.1038/nn.4310

described above. This shuffling procedure was repeated 1,000 times for each neuron per session. Cells in which the 2D correlation of one of the projections exceeded the 95% confidence interval, i.e. the correlation was lower than would be expected by chance, were classified as 'shape-change' neurons; similarly, cells in which the firing-rate change index exceeded the 95% confidence interval were classified as 'rate-change' neurons (see **Fig. 1e** and **Supplementary Fig. 10b**). For cells recorded over multiple sessions, we chose the directional classification of the session with the highest number of spikes. For cells that were classified as significantly directional, the two directions were further regarded as two separate cells in the remapping analysis (as is customary in the rodent literature[23,37]).

This analysis was conducted for both pyramidal cells and interneurons. Previous studies in rodents reported that CA1 interneurons exhibited directional selectivity mostly via rate changes between running directions[45], but here we found that the shape of the (broad) spatial tuning of CA1 interneurons in the bat also changed significantly between flight directions, in 64% of the interneurons (see **Supplementary Fig. 10b**).

Spatial information, sparsity and coherence. The Skaggs spatial information is a measure of the degree to which the firing of an individual cell is spatially specific[46]. We used the spatial information as our main measure to determine whether a neuron was a place cell or not (see above); and additionally, we used it to compare the spatial resolution of a single cell between vision-based and echolocation-based conditions (see below). The spatial information, in bits per spike, was computed from the smoothed 2D firing-rate map of each cell, as described previously[8,10]:

$$\sum p_i (r_i / \bar{r}) \log_2 (r_i / \bar{r})$$

where r_i is the firing rate of the cell in the ith bin of the 2D firing-rate map, p_i is the probability of the animal being in the ith bin (time spent in ith bin ÷ total session time), $\bar{r}$ is the overall mean firing rate and i iterates over all visited 2D bins (pixels). The spatial information index is high for neurons with high spatial selectivity.

To assess the compactness of place fields, we used two additional measures, spatial coherence and sparsity. Spatial coherence[8,47] is the correlation between the firing rates in the original firing map and the firing rates averaged across the eight neighbors of each bin. The coherence was computed from non-smoothed maps and was Fisher z-transformed to facilitate comparisons with previous studies[47]. Sparsity[48] is equal to

$$\left(\sum p_i r_i\right)^2 / \sum p_i r_i^2$$

Sparsity values are bound between 0 and 1. Note that, by definition, a place field with good spatial selectivity is indicated by high values of spatial information and coherence but low values of sparsity.

Remapping index. To analyze remapping, we separated the directional cells into the two flight directions and treated each direction separately. The remapping index was defined as $1 - r_{2D}$, where the 2D Pearson correlations, r_{2D}, were computed between vision and echolocation sessions and were averaged across the two vision sessions and averaged across the xy and xz projections. Only 2D pixels that were well sampled in both the Light and the Dark sessions (time spent > 150 ms) were included in this correlation calculation. The remapping index was computed only for cells that had both >25 spikes in one of the vision-based sessions, exhibited a stable spatial representation between the two vision (Light) sessions (correlation of 2D firing-rate maps for [Light, Light′] sessions: $r > 0.5$ in at least one of the projections), and had > 20 spikes in the echolocation-based session. This same inclusion criterion was applied to both CA1 neurons and subiculum neurons. Of the cells that had stable spike-sorted clusters (stable from the first to the last session), 63% of the pyramidal cells in CA1 and 38% in subiculum passed the tuning stability criterion; this result is in line with studies in rats that reported that subicular cells tend to be less functionally stable than CA1 cells[20]. The distribution of remapping indices of the entire cell sample was compared with the distribution of remapping indices expected by chance, by shuffling the cells that were active in both conditions (vision and echolocation) and calculating the remapping index for all nonidentical pairs of cells in vision versus echolocation[29,49] ('cell shuffling'). We calculated the shuffled distribution separately for CA1 pyramidal cells, subiculum pyramidal cells and CA1 interneurons (**Supplementary Fig. 6**). These shuffled distributions represent the expected similarities between firing-rate maps of unrelated neurons in our cell sample, and therefore they represent the distributions expected for completely random global remapping[29,49].

These remapping results were robust to the choice of the threshold for correlation value between the [Light, Light′] sessions: using a threshold of $r > 0.3$ (instead of $r > 0.5$), added only eight neurons to the data set, and the results of the statistical tests remained unchanged (Kolmogorov-Smirnov test comparing the probability distributions as in **Fig. 2j**: $P = 0.45$).

Sharpening index. For those cells that were active (>25 spikes per session) in the echolocation-based session and in at least one of the vision-based sessions, we calculated a sharpening index as follows:

$$\frac{\text{vision based spatial information} - \text{echolocation based spatial information}}{\text{vision based spatial information} + \text{echolocation based spatial information}}$$

The spatial information was computed for the 2D firing-rate map in the xy projection. If both of the vision sessions had >25 spikes, we used the average spatial information from both sessions as the vision-based value. In the insets in **Figures 4b**,**c** and **5c**, we recalculated the spatial information in each session by taking only those 3D voxels that behaviorally overlapped between the Light and Dark sessions (i.e., voxels that had sufficient time spent during both Light and Dark sessions); the spatial information was then computed over the 2D firing-rate maps (xy projection), as before.

For **Supplementary Figure 7a**,**b**, we computed similar sharpening indexes using the sparsity and coherence as additional measures of place field compactness.

Simulations of place cell models. We simulated three different models of place cells.

BVC model simulation. These simulations used parameters as in ref. 30, but varied the values of σ_d (distance resolution) and σ_{ang} (angular resolution). In **Supplementary Figure 8a**, these values were as follows: top, σ_d = 10 cm, σ_{ang} = 11°; bottom, σ_d = 12 cm, σ_{ang} = 17°. We used a 61 × 61 cm arena size in the BVC simulations.

View-based model simulation. These simulations were based on ref. 31. The view-based model was simulated using input images blurred to various levels (**Supplementary Figure 8c**). The baseline image used had a resolution of 500 × 180 pixels (**Supplementary Fig. 8c**, top), whereas the blurred image was smoothed with a 10-pixel Gaussian filter (**Supplementary Fig. 8c**, bottom).

Attractor network model simulation. We considered a network encoding a 1D circular track, to avoid boundary effects. A unit in the network represents a population of neurons with highly overlapping place fields. A unit with a place-field at angle $\theta \in [0, 2\pi)$ on the circular track is described by its firing rate at time t, $m(\theta, t)$, which follows the dynamics

$$\tau \dot{m}(\theta,t) = -m(\theta,t) + f(I_R(\theta,t) + I_E(\theta,t))$$

$f(I) = g[I]_+$ is a threshold-linear f–I curve. The input current to a unit is the sum of a recurrent contribution, $I_R(\theta, t)$, and an external contribution, $I_E(\theta, t)$. The recurrent contribution is

$$I_R(\theta,t) = \frac{1}{N} \sum_{\theta'} W(\theta,\theta') m(\theta',t) \quad (1)$$

where the sum extends over the N units equally spaced on the circle. The synaptic strength depends on the distance between the locations assigned to the units:

$$W(\theta,\theta') = J_1 \cos(\theta - \theta') - J_0 \quad (2)$$

where J_1 measures the strength of the location-specific (spatial) interaction and J_0 corresponds to a uniform feedback inhibition.
The external current contains three terms:

$$I_E(\theta,t) = I + I_L[1 + \cos(2\pi f_\Theta t)]\cos(\theta - \theta_{ext}(t)) + \eta(t) \quad (3)$$

The first term, I, is a spatially uniform and stationary current. The second term is a place-specific input with a temporal modulation at frequency f_Θ (mimicking the sampling rate of the sensory input); I_L denotes half of the maximum amplitude of

this input, at the location of the simulated animal $\theta_{ext}(t)$. The third term represents an Ornstein-Uhlenbeck process with a time constant $\tau_n = 20$ ms driven by white noise with a s.d. of $\sigma_n = 5$ Hz. The simulated animal position evolves according to

$$\theta_{ext}(t) = vt + \xi(t)$$

v is the speed of the simulated animal, and $\xi(t)$ is a delta-correlated Gaussian process with average $\langle \xi(t) \rangle = 0$ and variance $Var(\xi(t)) = \sigma^2$. The s.d. of this process is assumed to represent the resolution of the sensory input.

The parameters used were $\tau = 10$ ms, $J_1 = 15$, $J_0 = 15$, $g = 1.5$ Hz, $I = 2$ Hz, $I_L = 1$ Hz, $v = 1$ rad s^{-1} and $N = 200$.

The model equations were numerically solved using the Euler-Maruyama method (time step: d$t = 1$ ms). In order to obtain an estimate of the place field size, for a given set of parameters we simulated the dynamics for 1,000 trials. In each trial the virtual animal ran at a constant speed for 3 laps in the circular environment. The place field size of each unit in the network was estimated using Gaussian fitting.

We repeated this numerical analysis of the continuous attractor model for a wide range of input-noise values, which showed that degradation of the sensory inputs does degrade the place tuning, but this effect was very small over the tested range of parameters (**Supplementary Fig. 9a**).

To establish the robustness of our simulation results, we tested the effect on place tuning of a number of manipulations of cellular and network properties and of external input properties. (i) We compared different sensory sampling rates, corresponding to echolocation versus vision: we used an 8-Hz rate, which is typical for echolocation[16,17], and compared it to a 40-Hz rate, which is typical for vision (the flicker fusion limit[50]; see **Supplementary Fig. 9b**). (ii) We varied the time constant of integration of the single units (τ) at equally spaced values ranging from 5 ms to 200 ms (**Supplementary Fig. 9c**) and (iii) varied the temporal correlation of the noise (τ_n) from 5 ms to 200 ms (**Supplementary Fig. 9d**). (iv) The noise term in equation (3) was replaced by a spatially and temporally correlated term $\eta(\theta, t)$ (ref. 51; see **Supplementary Fig. 9f**). The scale of the exponentially decaying spatial correlation was $\lambda = 0.2$ rad; the time scale of the temporal correlation was the same as was used to produce the results in **Supplementary Figure 9a** ($\tau_n = 20$ ms). (v) Quenched noise was added to the synaptic coupling in equation (2), $W(\theta, \theta') = J_1[\cos(\theta - \theta') + z(\theta, \theta')] - J_0$ (ref. 52; see **Supplementary Fig. 9g**). The noise $z(\theta, \theta')$ was spatially uncorrelated, with average $\langle z(\theta, \theta') \rangle = 0$ and variance $Var(z(\theta, \theta')) = 1$. (vi) We endowed synapses in the network with short-term synaptic depression[32] (see **Supplementary Fig. 9e**). The recurrent contribution to the current (equation (1)) in this case was

$$I_R(\theta,t) = \frac{1}{N}\sum_{\theta'} W(\theta,\theta')m(\theta',t)x(\theta',t)$$

where $x(\theta, t)$ denotes the available fraction of synaptic resources at the synapses where the presynaptic unit has a preferred angle θ (i.e., a place field at angle θ on the circular track). This synaptic variable follows the dynamics

$$\dot{x}(\theta,t) = \frac{1 - x(\theta,t)}{\tau_R} - Ux(\theta,t)m(\theta,t)$$

τ_R is the time constant of recovery from depression and U is the release probability at the synapse. The parameters used in this case were $\tau = 10$ ms, $J_1 = 30$, $J_0 = 15$, $g = 1$ Hz, $I = 5$ Hz, $I_L = 5$ Hz, $v = 1$ rad s^{-1}, $\tau_R = 800$ ms, $U = 0.8$, $N = 200$.

Statistical methods. All data analysis, simulations and statistical analysis were performed in MATLAB (MathWorks), using custom MATLAB code. Computer code will be available upon request from the correponding author.

Population means were compared by using two-tailed t-tests, except a few cases where the normality of the data was uncertain, and then we used non-parametric tests, as stated in the appropriate locations. Distributions were compared using the Kolmogorov-Smirnov test. For determining significance of spatial information for place fields and significance of place-field directionality, we employed a shuffling analysis, as described above. Data collection and analysis were not performed blind to the experimental conditions. No statistical methods were used to predetermine sample sizes, but we note that our sample sizes are similar to those reported in previous studies in rats[4,29,49].

Histology. Histology was done as described previously[8,10]. In brief, at the end of recordings, the bats were anesthetized, and in some cases electrolytic lesions (DC positive current of 30 μA, 15-s duration) were made to assist in the precise reconstruction of tetrode positions. The bat was then given an overdose of sodium pentobarbital and, with tetrodes left *in situ*, was perfused transcardially using 4% paraformaldehyde. The brain was removed and thin coronal sections were cut at 30 μm intervals. The sections were Nissl-stained with cresyl violet and were photographed to determine the locations of tetrode tracks in the CA1 or subiculum.

A **Supplementary Methods Checklist** is available.

44. Schmitzer-Torbert, N., Jackson, J., Henze, D., Harris, K. & Redish, A.D. Quantitative measures of cluster quality for use in extracellular recordings. *Neuroscience* **131**, 1–11 (2005).
45. Wilent, W.B. & Nitz, D.A. Discrete place fields of hippocampal formation interneurons. *J. Neurophysiol.* **97**, 4152–4161 (2007).
46. Skaggs, W.E., McNaughton, B.L., Wilson, M.A. & Markus, E.J. in *Advances in Neural Information Processing Systems 5* (eds. Hanson, S.J., Cowan, J.D. & Giles, C.L.) 1030–1037 (Morgan Kaufman, San Mateo, California, USA, 1993).
47. Muller, R.U., Kubie, J.L. & Ranck, J.B. Jr. Spatial firing patterns of hippocampal complex-spike cells in a fixed environment. *J. Neurosci.* **7**, 1935–1950 (1987).
48. Skaggs, W.E., McNaughton, B.L., Wilson, M.A. & Barnes, C.A. Theta phase precession in hippocampal neuronal populations and the compression of temporal sequences. *Hippocampus* **6**, 149–172 (1996).
49. Alme, C.B. *et al.* Place cells in the hippocampus: eleven maps for eleven rooms. *Proc. Natl. Acad. Sci. USA* **111**, 18428–18435 (2014).
50. Healy, K., McNally, L., Ruxton, G.D., Cooper, N. & Jackson, A.L. Metabolic rate and body size are linked with perception of temporal information. *Anim. Behav.* **86**, 685–696 (2013).
51. Goldberg, J.A., Rokni, U. & Sompolinsky, H. Patterns of ongoing activity and the functional architecture of the primary visual cortex. *Neuron* **42**, 489–500 (2004).
52. Itskov, V., Hansel, D. & Tsodyks, M. Short-term facilitation may stabilize parametric working memory trace. *Front. Comput. Neurosci.* **5**, 40 (2011).

doi:10.1038/nn.4310

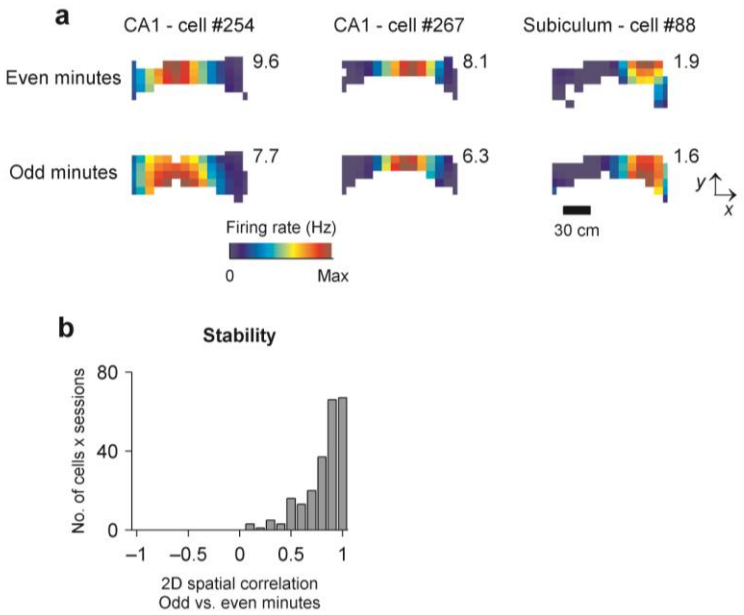

Supplementary Figure 1

Stable hippocampal place-fields in bats shuttling along a linear flyway

(**a**) Examples of 3 cells, showing the 2D projections of the firing-rate map, calculated for the even minutes of the session (top) and for the odd minutes (bottom). Peak firing rate is indicated for each rate-map. Note the place-field location is very stable. (**b**) Distribution of correlation coefficients between odd-minute and even-minute firing rate maps, for all the place cells. Mean correlation: r = 0.80, indicating high stability of the place fields.

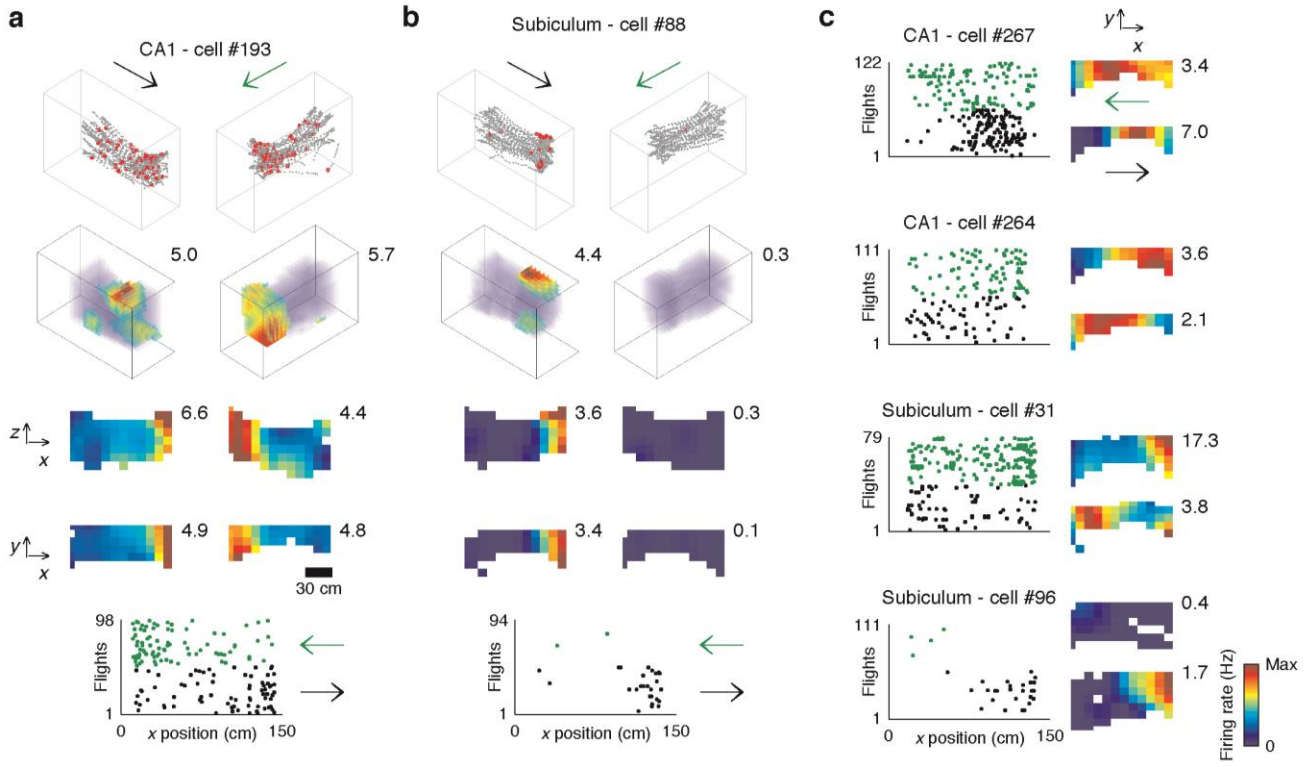

Supplementary Figure 2

Directionality of place-cell firing in CA1 and subiculum in bats shuttling along a linear flyway

In tasks involving goal-directed, stereotyped trajectories, the activity of rodent hippocampal place-cells differs depending on the animal's movement direction[25]. In our experimental paradigm, many bat place-cells showed clear directional tuning – despite the fact that trajectories were not strictly repeating, because bats were flying between 9 possible positions at each end of the flyway (81 combinations; Fig. 1a). Directional tuning properties had one of the following characteristics: (i) a different place-field location for each flight direction (e.g., panel **a**); (ii) a different firing-rate in each direction, including some cells that shut-down completely in one of the directions (e.g., panel **b**); (iii) or combinations of tuning-shape- and rate-changes (e.g., panel **c**, cell #31). These directional differences were seen in both CA1 and subiculum cells (see population summary in Fig. 1e). (**a**) Example cell in CA1, exhibiting different place-fields for both flight directions. (**b**) Example cell in subiculum, exhibiting shut-off in one of the flight directions**.** Columns in (**a**-**b**) depict left-to-right flights or right-to-left flights (see arrows), for a single behavioral session. Rows: (1) Raw data (gray lines, trajectories; red dots, spikes); (2) 3D firing-rate maps. (3) 2D firing-rate maps: *xz* projection; (4) 2D firing-rate maps: *xy* projection; (5) Raster showing *x*-position of spikes (*x*-axis) for all flights (*y*-axis); green, spikes during right-to-left flights; black, left-to-right flights. Firing-rate maps are color-coded, with blue corresponding to zero and red to peak firing-rate (indicated on the right; except panel **b**-right, where colors are according to the color-scale of the active direction on the left). (**c**) Additional 4 examples of directional cells (2 from CA1 and 2 from subiculum); plotted as in panels **a**-**b**.

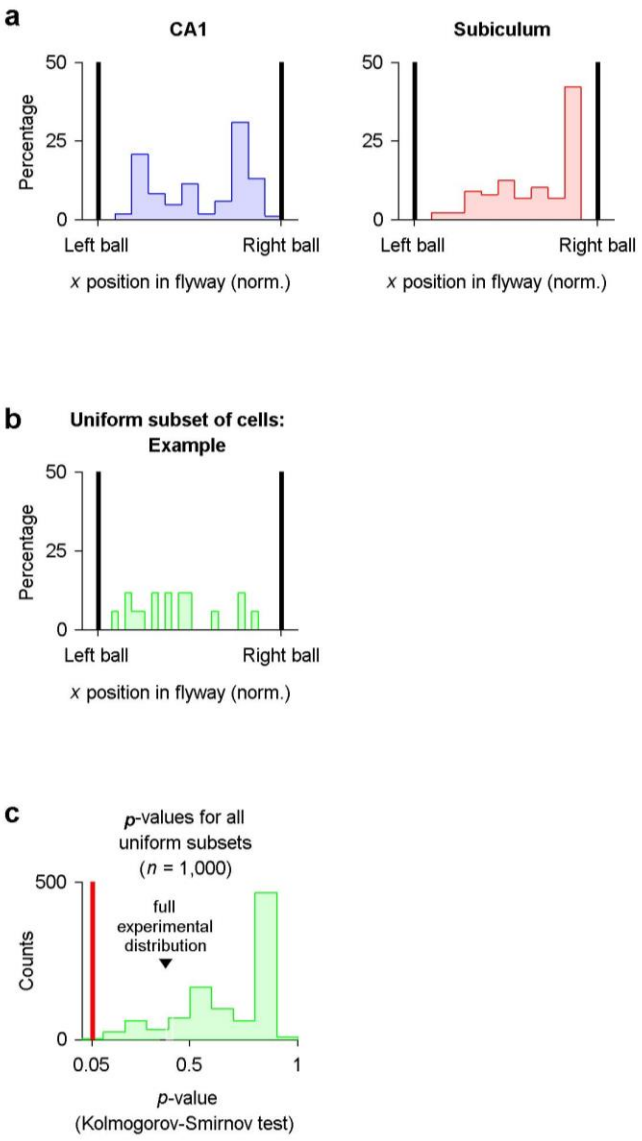

Supplementary Figure 3

Distribution of place-field locations along the linear flyway

(**a**) Histograms of the normalized locations of the peak-firing rate along the flyway. Left, CA1 (n = 168 cells × sessions); Right, subiculum (n = 88). We included those cells and behavioral sessions that had > 25 spikes and exhibited significant spatial information based on shuffling criteria (i.e., place cells; see Online Methods). (**b-c**) To verify that the non-uniform distribution of CA1 place-field locations in panel **a** did not affect the statistical test for orthogonality of CA1 hippocampal remapping (Fig. 2j, Kolmogorov-Smirnov test), we conducted the following control analysis: We drew 1,000 subsets of uniformly-distributed place-field locations from the real data, by randomly assigning one cell to each spatial bin, with the bins being uniformly-distributed (25 bins uniformly-distributed between the left and the right ball). (**b**) An example of the histogram of place-field locations for one of these uniformly-drawn subsets of cells. (**c**) *P*-value distribution for all the 1,000 shuffled uniform subsets: for each of the 1,000 subsets we used a Kolmogorov-Smirnov test to compare the true distribution of remapping indices for this subset of neurons, versus the distribution of remapping indices computed for all the non-identical cells (which is the expected distribution for global remapping). This is the same type of calculation that we did for the full dataset (Fig. 2j). Note that all the 1,000 subsets of neurons with uniformly-distributed place fields yielded *P*-values higher than the 0.05 threshold (panel **c**, the entire green distribution is above the red line). Thus, we conclude that the non-uniform distribution of

place-field locations does not affect the basic result of Fig. 2j – i.e., there is place-field orthogonalization between the vision-based and echolocation-based sessions, with place field positions shifting completely randomly – namely, a global remapping. Inverted arrowhead denotes the *P*-value for the original full dataset in Fig. 2j ($P = 0.39$).

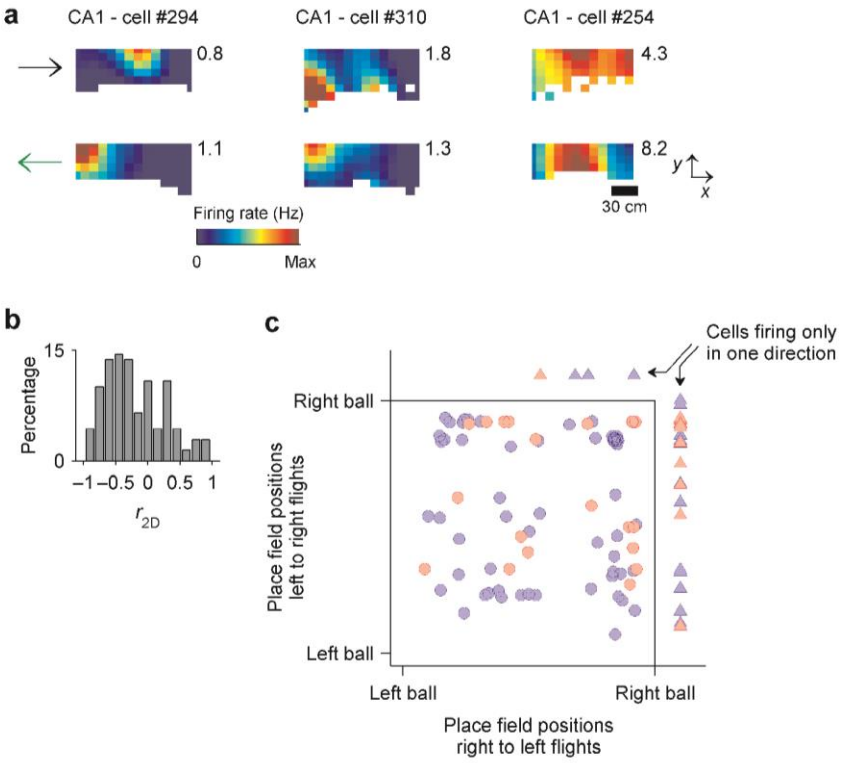

Supplementary Figure 4

No systematic relation between place-field positions in the left-right flight direction versus the right-left flight direction

A previous study in rats running along a linear track (in virtual reality, VR) found that hippocampal CA1 cells in VR represent distance along the track rather than absolute allocentric location – a phenomenon termed distance coding, or "disto-code"[27]. Here we examined whether a similar phenomenon might exist in flying bats – but we found no evidence for such 'disto-coding' in our data, neither in CA1 nor in subiculum. (**a**) Examples of firing-rate maps for 3 cells which fired in both flight directions ('bi-directional cells'), and whose place-fields occurred at *different distances* from the start-location of the flight when comparing left-right flights versus right-left flights (rows). Note that the place field in cell #310 was tuned to different locations on the y-axis in the two flight-directions, and that cell #254 had clear spatial tuning only during right-to-left flights. (**b**) Distribution of correlation coefficients computed between the 2D firing-rate maps (*xy* projection) for right-to-left flights versus the *inverted* map for the opposite, left-to-right flight direction (inverted along the *x*-axis). If there was disto-coding in our data, these correlations should be strongly shifted toward *positive* values[27]; however, our data showed an opposite, slightly negative bias (median r_{2D} = –0.28) – arguing against disto-coding in our data. (**c**) Scatter plot of normalized place-field locations for the two flight directions – for all CA1 cells (blue) and subiculum cells (red). *x*-axis: place-field location for right-to-left flights; *y*-axis: place-field location for left-to-right flights. Circles, bi-directional cells; triangles, cells firing only in one flight-direction. Dots were slightly jittered for visualization only, to prevent overlay of dots. Note the absence of a negatively-correlated diagonal band in this scatter-plot – a band that would be predicted for disto-coding[27] – which argues against a disto-code in our bat data.

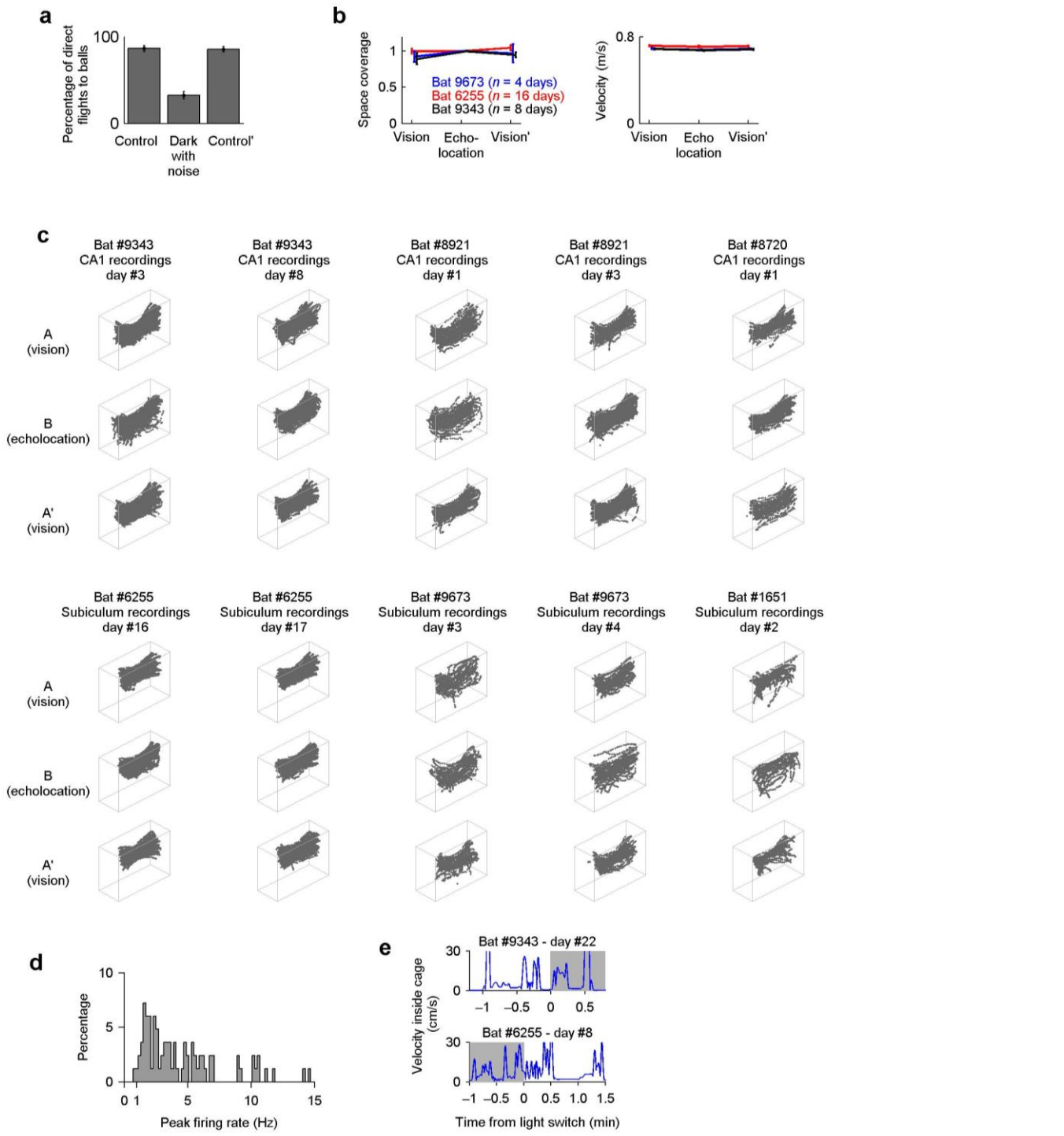

Supplementary Figure 5

Behavioral and neural controls for remapping experiments

(**a**) Degradation of behavioral performance when a broadband noise was broadcasted to mask echolocation calls in complete darkness. These measurements were done in a separate behavioral experiment, in which we tested whether bats (n = 3) could find their way to the target ball in the dark while we broadcasted the broadband noise. Ventilators were used to eliminate odor cues in all sessions. This 'dark+noise' manipulation caused a dramatic drop in behavioral performance compared to the standard sessions (compare the middle bar [dark+noise] to the flanking controls [two repeats of a control session]). Performance was quantified as the percentage of direct flights-to-balls. For the control condition, we pooled sessions where the control was dark-without-noise and sessions in which the control was light-with-noise. The drop in performance in the 'dark+noise' condition was very significant – the bats were basically repeatedly crashing and flying astray in the 'dark+noise' condition (paired t-test comparing performance in 'dark+noise' sessions [n = 14] versus control sessions: $P < 10^{-7}$). (**b**) Left − space coverage is very similar between same-day light and dark sessions (paired t-test comparing spatial spread in vision [average of two sessions] versus echolocation conditions: $P > 0.1$ for all bats; see Online Methods). Right − average maximal velocity across flights is compared between same-day sessions. The velocity differences between light and dark were very small − 2%, 3% and 6% velocity differences for bats # 9343, 6255 and 9673, respectively − although these small differences were significant for 2 of the 3 bats (paired t-test for the 3 bats: P = 0.02, P = 0.003 and P = 0.23, respectively). Error bars, mean ± s.e.m. Data shown for implanted bats which had at least 4 recording days. (**c**) Raw behavioral data of flight trajectories (gray lines) for the 3 sessions (rows); shown are example days for all the bats participating in vision-versus-echolocation analysis. These raw data illustrate the similar flight patterns in light and dark sessions. (**d**) Distribution of peak firing-rates for all the pyramidal cells that were included in the remapping analysis – using 2D firing-rate maps (xy projection), taking for each cell the session with the highest firing-rate (pooling n = 56 cells in CA1 and n = 27 cells in subiculum). Note that for almost all cells, the peak firing-rate was > 1 Hz, and for many cells it was > 5 Hz. (**e**) Bats were awake and moving around the time of the light-switch, just before the flight-session began. Shown are examples of behavioral data depicting bat movement velocity around the time of the light-switch (2 bats, 2 different days): the top example shows switch from light to dark; the bottom example shows a switch from dark to light. Time 0, light-switch; gray rectangle denotes the dark condition.

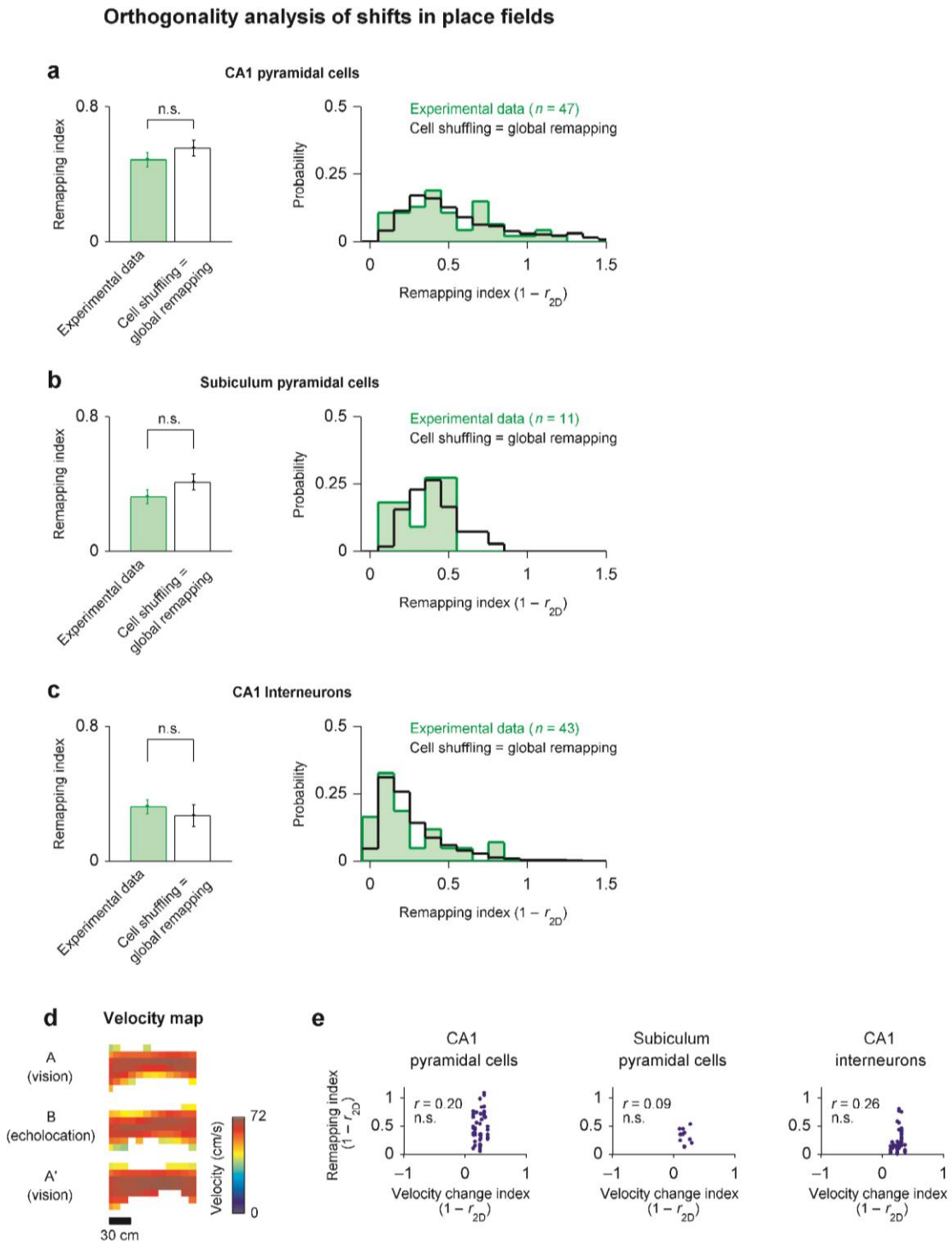

Supplementary Figure 6

Distribution of remapping indices for the experimental data is not significantly different from that expected from completely random global remapping

To test if the hippocampal maps under vision and echolocation are truly orthogonal (independent) for cells active in both conditions, we

compared the empirical distribution of remapping indices for these cells, versus a 'cell-shuffling' distribution. For the cell-shuffling, we computed remapping-indices between all pairs of *different* cells: this shuffled distribution represents the expected differences between firing-rate maps of *unrelated* neurons in our cell-sample – and therefore represents the expected distribution for completely random 'global remapping' [29] (see Online Methods). (**a**) CA1 pyramidal cells (n = 47). (**b**) Subicular pyramidal cells (n = 11). (**c**) CA1 interneurons (n = 43). In all cases: Left column – Comparing the mean remapping indices between experimental data (green) and the cell-shuffling distribution (black). Right column – The full experimental distribution of remapping-indices (green) versus the cell-shuffling distribution (black). Kolmogorov-Smirnov tests comparing the probability distributions: P = 0.39, P = 0.42 and P = 0.17 for **a**, **b** and **c**, respectively – signifying that the distribution of actual remapping indices was *not* significantly different from that expected from completely random global remapping. (**d**) Example of the spatial velocity profiles ('velocity maps') for one recording day, calculated with the same spatial bins as the firing-rate maps; each bin here depicts the mean velocity at that spatial location. Color scale goes from zero velocity (blue) to peak velocity (red, value indicated). Note the similarity in velocity maps between vision and echolocation sessions. (**e**) Plots of the remapping index (which was computed as in Fig. 2) versus the velocity-change index (which was computed in an analogous manner, over the velocity maps) – for CA1 pyramidal cells (left), subiculum pyramidal cells (middle) and CA1 interneurons (right). Note that the velocity-change indices were concentrated near zero – i.e. there were essentially no differences in velocity-maps between the vision and echolocation sessions. Moreover, note the remapping index was not correlated with the velocity-change index, for any of the three neuronal populations – arguing against the notion that velocity differences could explain the observed neural remapping.

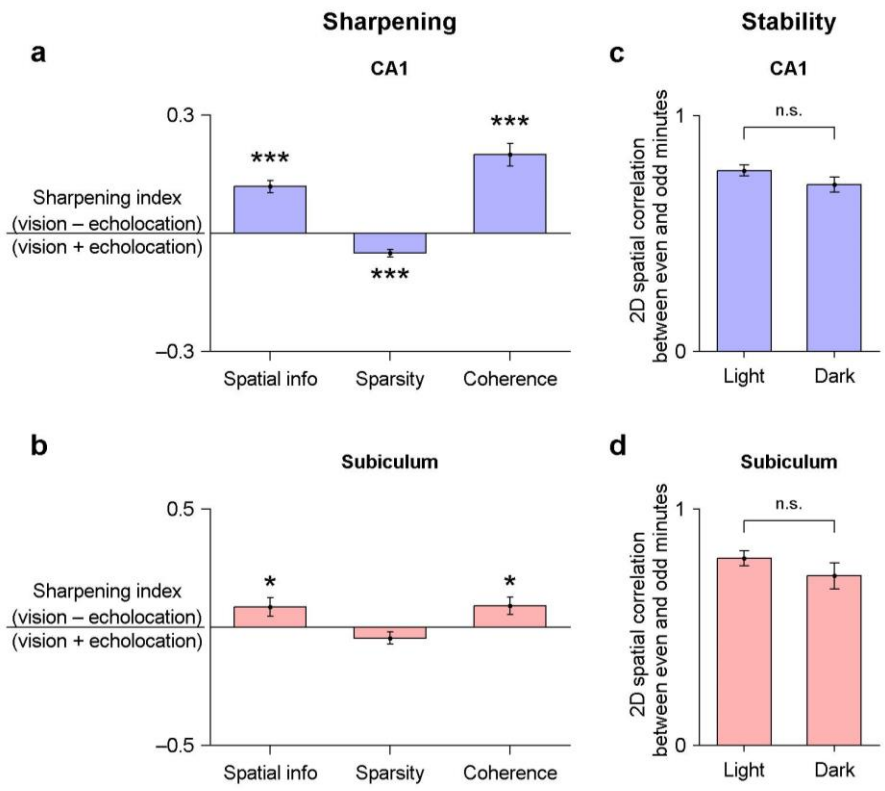

Supplementary Figure 7

Spatial representation sharpens under vision versus echolocation

(**a-b**) Population summary of the sharpening index, which compares place-field compactness under vision versus echolocation (see Online Methods), plotted separately for place-cells in CA1 (panel **a**: $n = 48$ cells) and in the subiculum (panel **b**: $n = 16$ cells). This analysis showed that the spatial resolution of CA1 cells is higher under vision than under echolocation (and a similar though weaker effect is observed also in the subiculum). Sharpening indices were computed here based on the spatial information index (left bars: same index as in Fig. 4b-c), as well as based on sparsity and coherence indices (middle and right bars; see Online Methods). Note that the sparsity index is expected to behave the opposite from the spatial-information and coherence indices (by definition, lower sparsity corresponds to higher spatial information and higher coherence). '*', $P < 0.05$; '***', $P < 10^{-5}$ (*t*-test). (**c**-**d**) Firing-rate map stability (correlation between maps computed for odd-minutes versus even-minutes), in light and dark sessions, for CA1 (**c**) and subiculum (**d**). There was no significant difference between map stability in light versus dark sessions, in either **c** or **d** (*t*-test, $P > 0.12$ for both **c** and **d**).

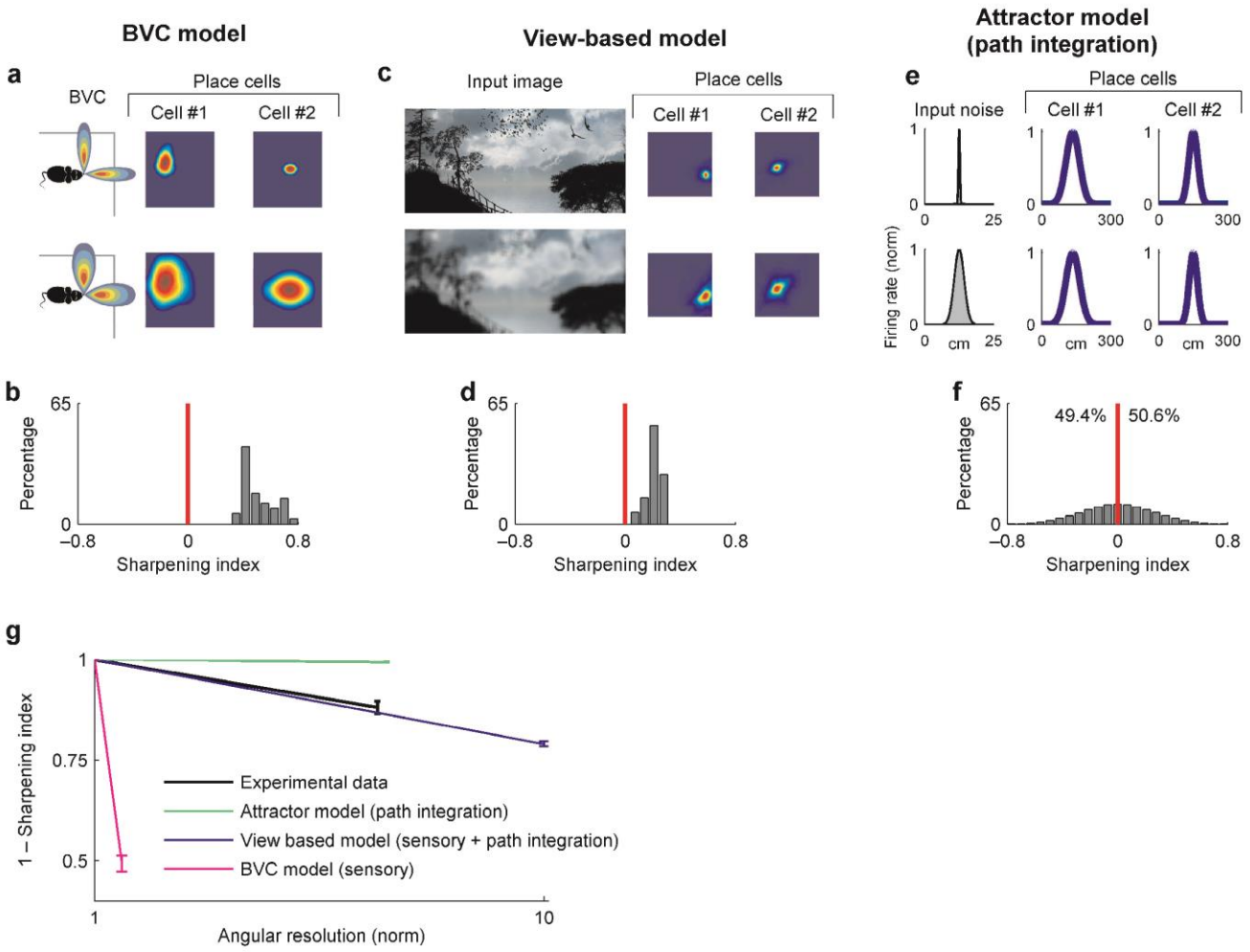

Supplementary Figure 8

Simulations of 3 models of place cells support a combination of sensory-based and attractor network models

Theoretical models of place cells can be classified (among other ways) according to the relative importance they assign to external sensory inputs versus self-motion cues ('path integration'). We can test the importance of the external sensory input in a selection of commonly-used models by degrading the sensory resolution of the input in each model, and computationally test the effect of this sensory degradation on simulated place-cell tuning. We can then compare these predictions to the experimentally-observed differences in place tuning under the different sensory resolutions for echolocation versus vision (2° versus 0.3°). These simulations suggest that the spatial-sharpening effect is best explained by combining sensory-based and path-integration mechanisms. (**a-b**) A widely-used sensory-based model – the 'boundary vector cell' (BVC) model[30, 33]. In this model, each 'boundary cell' is tuned to a specific distance and direction from geometric boundaries, forming a band of activity. The intersection between the activity bands of several boundary-cells forms a place-field. (**a**) Left: schematic of boundary-vectors. Right: simulated place-fields (columns: cells #1 and 2) for different sensory resolutions (rows). These simulations used parameters as in ref. 30, but varied the values of σ_d (distance resolution) and σ_{ang} (angular resolution): Top, σ_d = 10 cm, σ_{ang} = 11°; bottom, σ_d = 12 cm, σ_{ang} = 17°. Arena size, 61×61 cm. Note the dramatic increase in place-field size (bottom versus top) when degrading the BVC input resolution. (**b**) Distribution of sharpening index for the BVC model; plotted as in Fig. 4b. The distribution of sharpening-indices between the two sensory resolutions is strongly shifted to the right, predicting that spatial information should be reduced for the degraded sensory condition. (**c-d**) We repeated the same analysis as in (**a-b**) for a very different model – the 'view-based' model[31, 34], which uses as an input a realistic full retinal image combined with self-motion cues. We compared the sizes of simulated place fields for high-resolution visual input (top left) versus visual input with degraded angular resolution (simulation courtesy of Denis Sheynikhovich). (**c**) Two pictures were used as 'retinal image' inputs to the model: top image, no blurring (high resolution); bottom image (lower resolution) was blurred with a 10-pixel Gaussian filter. Right: simulated

place-fields (columns) for the two visual resolutions (rows). Note the mild increase in place-field size (bottom versus top) when degrading sensory input resolution. (**d**) Distribution of sharpening index for the view-based model. The simulations of the view-based model (**c-d**) showed the same qualitative direction of change as the BVC model simulations (**a-b**), and as observed in our experimental CA1 data (Fig. 4a-b) – although these two models differed substantially in the magnitude of the spatial-sharpening effect. (**e-f**) Third, we tested whether a sharpening effect will be observed in a continuous attractor network model, which is oftentimes considered as a computational mechanism for path integration[35]. For simplicity, we used a one-dimensional network, where the animal's position was modeled as a continuous variable on a circular track with a 50-cm radius (Online Methods). A combination of recurrent connections between excitatory neurons in this network, together with global inhibition, leads to the spontaneous formation of a localized bump of activity which moves with the animal (path integration), and thus results in spatially-localized place fields[35] (cells #1 and #2; Online Methods). To evaluate the effect of degraded sensory input in this model, we varied the standard-deviation (noise) of the input – according to the known biological sensory acuity of vision (0.3° noise: top) and echolocation (2° noise: bottom). (**e**) Left: two example inputs, modeling sensory acuity of 0.3° (top) and 2° (bottom); these sensory resolutions in degrees were transformed to cm via the 50-cm radius of the simulated circular track. Right: Simulated place-cells (columns) for the two sensory resolutions (rows). Note there is very little change in place-tuning under the two different sensory resolutions (compare top to bottom). (**f**) Distribution of sharpening index for the attractor model. The histogram is shifted very slightly but significantly to the right (*t*-test: $P < 10^{-9}$). (**g**) Comparing place-field blurring (1 – sharpening index) of the experimental data (black line) to predictions of 3 theoretical models (colored lines). The experimental data best match the view-based model[31, 34] (blue line), which is a hybrid model that uses a combination of sensory information (retinal image) and path-integration (self-motion). The normalized angular resolution was taken here as the ratio between angular resolutions simulated in panels **a**-**b** (BVC model) or in panels **e**-**f** (continuous attractor model); or was taken as the relative size of the blurring-filter (10 pixels: view-based model, panels **c**-**d**).

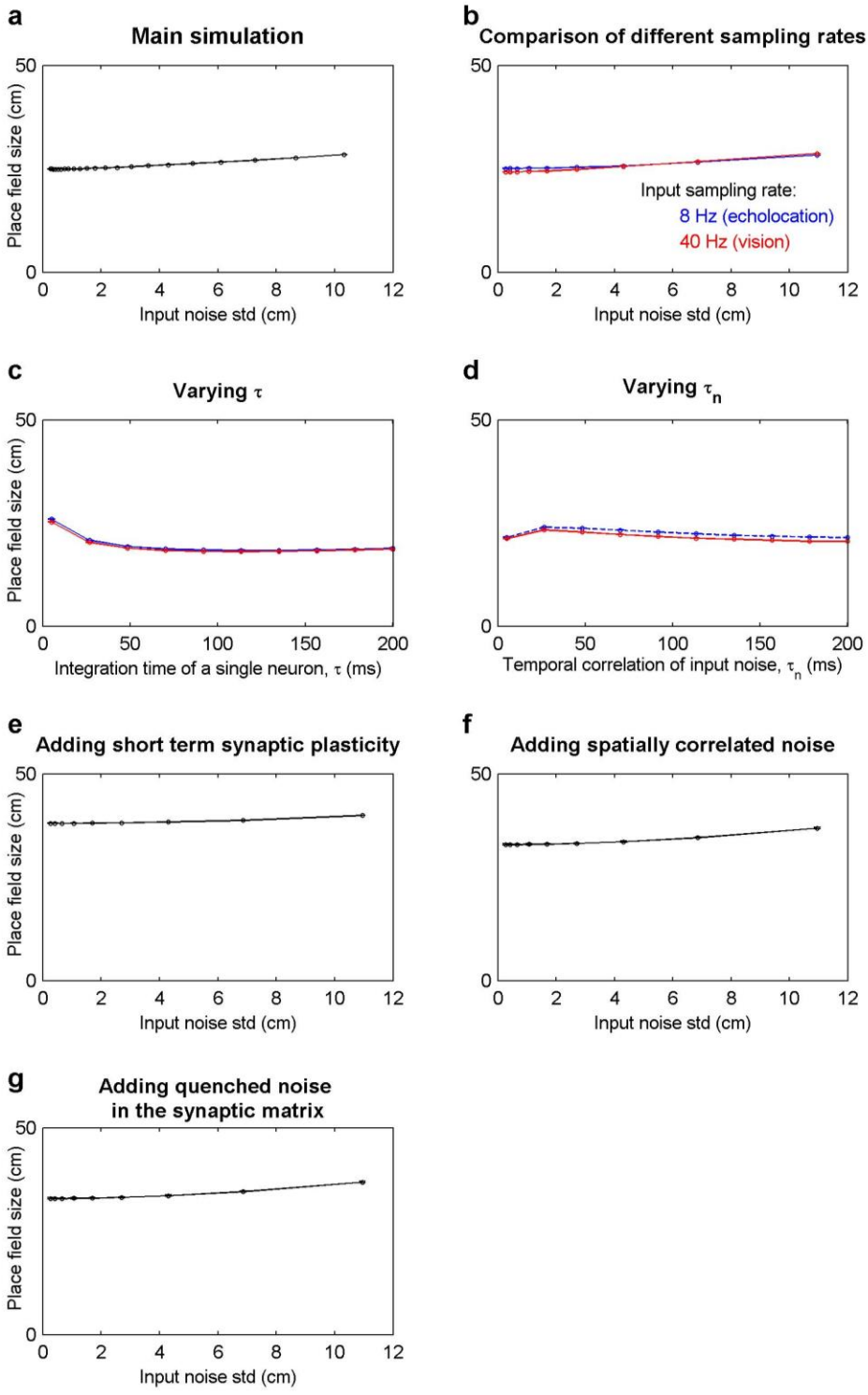

Supplementary Figure 9

Continuous attractor neural network model shows a very weak dependence of simulated place-field size on sensory-input resolution

Continuous attractor neural networks models were suggested as a computational mechanism for path integration[35.] Here we compared them to sensory-based models for place cell generation - by examining how well can these different classes of models explain our experimental results on place-field sharpening in light versus dark (main Fig. 4). In Supplementary Fig. 8 we showed that, in contrast to the BVC-model[30, 33] and the view-based model[31, 34], the place-field size in the continuous attractor model exhibits a very weak dependence on the sensory input resolution (see detailed explanations and simulations results for all models in Online Methods and Supplementary Fig. 8). To establish the robustness of these results for the continuous attractor model, we further tested the effect on place tuning of a number of manipulations of cellular and network properties and of external input properties – but, as shown in this figure, none of these manipulations changed the results. (**a**) Place field size slightly increased when the standard deviation (noise) of the input was increased. Each point represents the average of the place-field size measured for 200 neurons in the network, on 1,000 simulation repeats (see Online Methods). Sampling rate was 25 Hz (same sampling-rate as used in all the simulations shown in Supplementary Fig. 8e-g). (**b**) Sensory sampling rate had little effect on the results shown in panel **a** – we compared here an 8-Hz sensory-rate, typical for echolocation[16, 17], versus a 40-Hz rate, typical for vision ('flicker-fusion limit'[50]). Changing the single-cell integration time constant, τ (**c**) or the temporal correlation of the noise, τ_n (**d**), over a broad range of values of these time constants, did not have a substantial effect. The dependence of place-field size on sensory-noise remained very weak also when we added short-term synaptic plasticity[32] (**e**), or used spatially-correlated noise at the input[51] (**f**), or added quenched noise in the synaptic matrix[52] (**g**). See Online Methods for details of simulations.

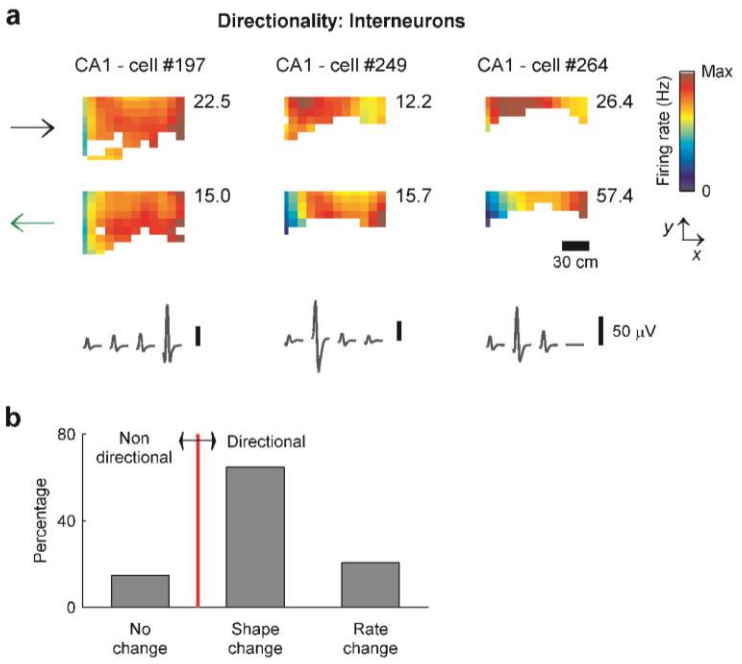

Supplementary Figure 10

Directionality of CA1 interneurons on the linear flyway

(**a**) Example interneurons (columns) exhibiting significantly different spatial tuning in the two flight directions: some cells exhibited a significant change in firing-rate between flight directions (left example), while other cells significantly changed their (broad) spatial tuning between flight directions (middle and right examples). Significance was based on a shuffling-test (see Online Methods). Shown are the *xy* projections of the 2D firing-rate map. Bottom: spike waveforms for these cells; scale bars, 50 μV. (**b**) Percentages of different kinds of directional tuning for CA1 interneurons (Online Methods).

Supplementary figure 11

a. An algorithmic perspective on hippocampal function

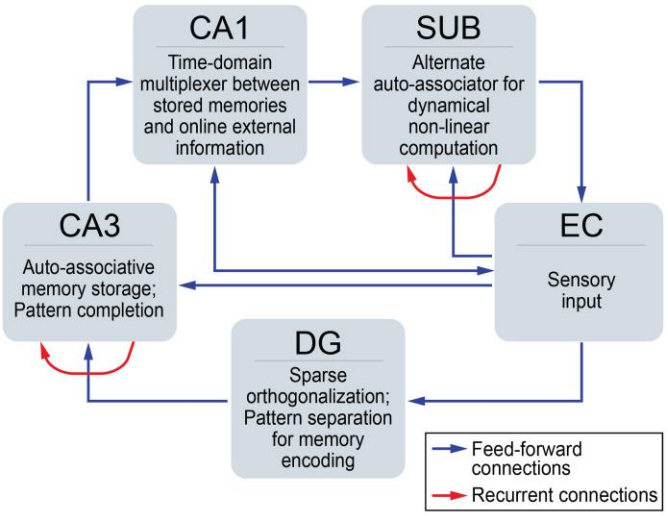

b. The 'cognitive atlas' hypothesis

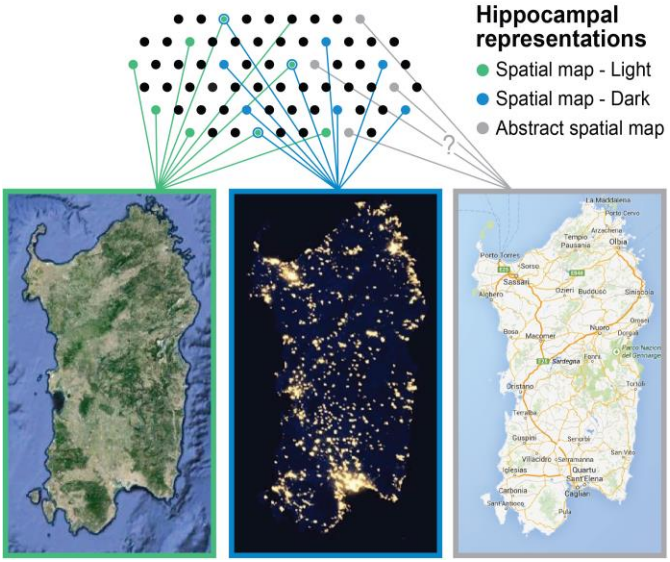

Supplementary Figure 11

Hypotheses

(**a**) An algorithmic perspective on hippocampal function posits that the subiculum acts as an alternate autoassociator (in addition to CA3), which could enable memory functions and non-linear dynamical processing when the information from entorhinal cortex (EC) bypasses the dentate gyrus (DG) and CA3 and is routed along the shortcut path: EC → CA1 → Subiculum (see Colgin et al., *Nature* 462, 353, 2009). This may explain the differences in remapping schemes between CA1 and subiculum that we found in our study. (**b**) Our 'cognitive atlas' hypothesis posits that the same space can be coded by several different maps. Two groups of neurons (which could be partially overlapping), depicted here as blue and green dots, may store separate cognitive maps for two different sensory conditions (see left map – green, and middle map – blue); a third group of neurons, depicted here as gray dots, may possibly code for an abstract map, independent of context (see right map – gray), although our data do *not* provide evidence for the existence of such an abstract map.